KING'S College LONDON

University of London

7CCYB060 Extended Research Group Project

A Toolkit For Tele-Operated Robotic Thrombectomy in Acute Stroke

Aaliyah Adesida, Jiaheng Wang, Shiyang Lu, Yitong Wang

Supervisors: Dr Thomas Booth, Ben Jackson & Dr S.M Hadi Sadati

Project Report
submitted in partial fulfilment of the
MRes in Healthcare Technologies and the MEng in
Biomedical Engineering

June 2024

Abstract

Mechanical thrombectomy is a procedure used to treat stroke. Studies have shown a direct correlation between reduced time taken to remove a clot from the brain, and more successful patient outcomes. There are a limited number of departments within the UK that can provide interventional mechanical thrombectomy as a service. If clinicians could perform mechanical thrombectomy in geographically remote locations through tele-operated robotics, the potential to treat a large number of patients quickly is amplified. The aim of this project was to create a research toolkit for the development of robotic mechanical thrombectomy with the main focus on the key step of navigation where guidewires and catheters are used to reach the clot from outside the patient. To achieve this, two haptic feedback controllers were designed and built, and two meshes spanning from the aorta to the middle cerebral artery bifurcation were extracted from patient data to allow robotic responders to drive guidewires in silico. Additionally, a reinforcement learning algorithm trained to navigate intravascularly, was developed to pave the way towards robotic autonomy. Exemplar results show that the reinforcement learning algorithm had a lower navigation time than human users of the haptic controllers, with means of 17.35s and 32.23s respectively for navigating to the Left Common Carotid Artery. In conclusion, we successfully built a toolkit for robotic mechanical thrombectomy and demonstrated some relevant use cases.

1 Background and Introduction

1.1 Motivations

Cerebrovascular incidents, colloquially known as strokes, affect 100,000 people in the UK each year [1]. Around 85% of strokes in the UK are ischaemic strokes [2], in which there is a blockage of blood flow within the brain.

During the treatment of stroke, a “Time is brain” strategy is common. Studies have shown that in the treatment of acute ischaemic stroke in general, endovascular treatment initiated within less than four hours of the stroke onset drastically improves patient outcomes [3]. Mechanical thrombectomy is widely viewed as the most effective method of treatment for occlusive stroke [4]. However, carrying out this procedure requires specialist facilities and highly-trained practitioners. As of June 2023, only 24 neuroscience centres provide mechanical thrombectomy services. Of those 24 centres, only four operate 24/7, three of which are in London, making the coverage geographically unequal.

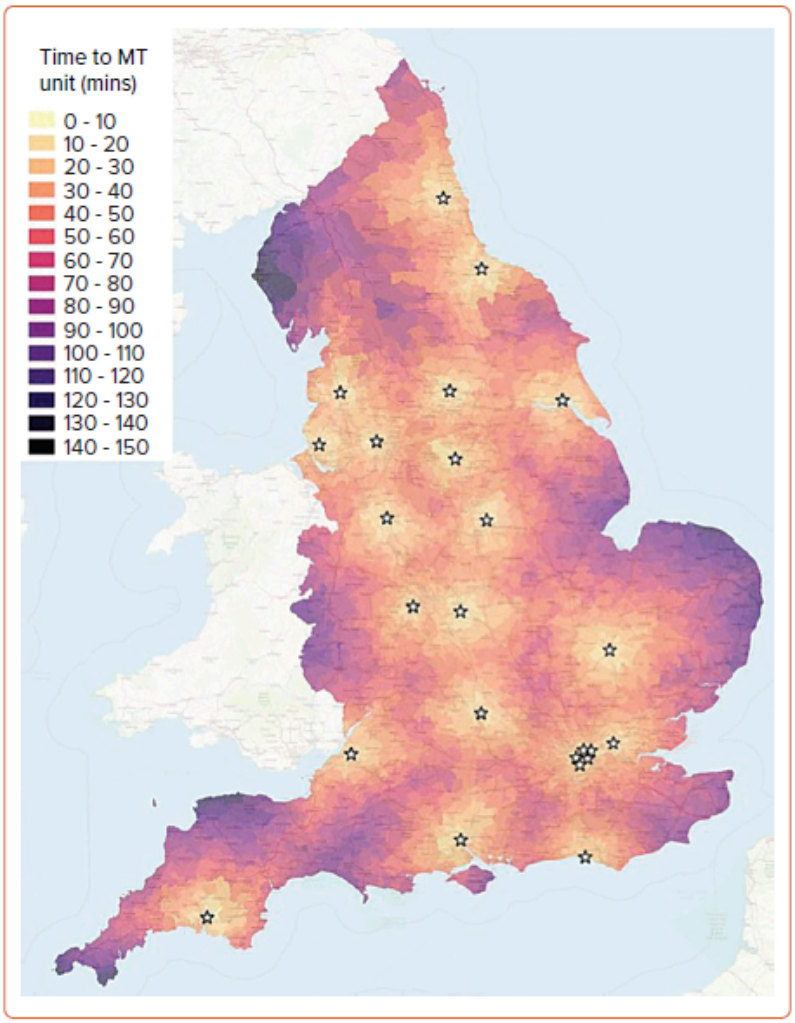

Figure 1: Heatmap showing the time taken in minutes to a centre capable of mechanical thrombectomy [5].

The time taken for treatment is longer than the travel time taken as patients require diagnosis through clinical assessment and imaging. The net result is few patients are ready for treatment within 4 hours which is disproportionately influenced by geography.

Given that the number of ischaemic stroke patients who receive emergency treatment in the UK is around 2% [5], there is a definite need for an increase in accessibility for these procedures. It is also important to maintain awareness that those of Black and South Asian Heritage are at greater risk of stroke [6] when discussing these issues. Furthermore, those from lower socioeconomic status overall have a higher risk of stroke, of higher severity and an increased chance of adverse outcomes [7].

1.2 Previous Works

One method for increasing access to mechanical thrombectomy that is currently being explored is the training of existing interventional cardiologists to perform mechanical thrombectomy, however, this is still being explored [5]. Other than that, several studies have also explored the simulation of the behaviour of flexible medical devices [8]. Despite these methods, previous studies surrounding robotically performed neurointerventional surgery have been carried out to determine the degree of manual assistance required to perform procedures. These studies have found that robotically performed procedures have significant chances of successfully benefiting patients, however, there was a lack of high-level evidence implying robotically performed procedures are as efficient as manual methods [9].

As we explore the potential of robotic surgery, it becomes important to delve into the specific technologies that enable these advancements. In the following sections, we describe several components relevant to the formation of a robotic mechanical thrombectomy toolkit.

1.2.1 Haptic Robotic Controllers

According to a systematic review carried out in 2021, a significant limitation in current robotic systems for interventional surgery is the lack of haptic feedback [9]. Providing tactile feedback to the operator is of utmost importance, across literature effectively relaying sensory information to the clinician is yet to be done. Controllers for endovascular systems often employ a device-mimicking approach, in which the controller movements directly replicate the operator's actions. However, there are instances of systems where the operator's movements are transformed, such as using a joystick to manipulate the catheter and guidewire [10].

The haptic controller in this study will mainly be improving from previous work [10]. The robotic controller described in this study provides two degrees of freedom; the user manipulates a cylindrical grip to slide the carriage along linear rails, controlling the advancement and retraction of catheters and guidewires. Additionally, the rotation of the grip controls the rotational degree of freedom of these instruments. Precise movement and feedback are enabled by rotary encoders attached to the linear and rotary axes, measuring the position of the controller. The haptic controller consists of motors which provide individualised force feedback for each degree of freedom, based on forces calculated at the catheter and guidewires distal tips.

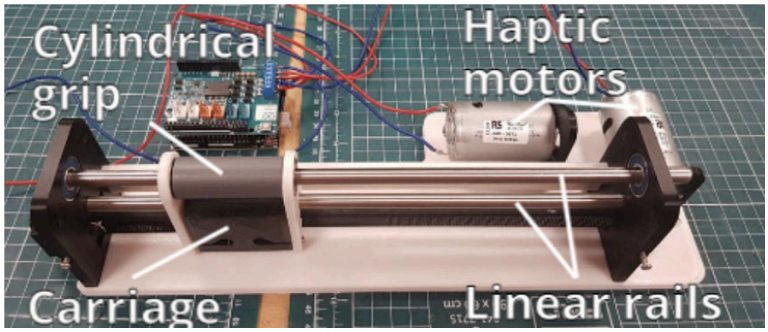

Figure 2: Haptic controller built by previous researcher [10]

However, this device currently exhibits several limitations that affect its surgical performance. It offers only two degrees of freedom (DOF), limiting the manoeuvrability necessary for thrombectomy procedures. Corrosion of the actuating rod impedes movement and reduces operational smoothness, adversely impacting the system's precision. High friction in the controller's movements results in a decreased sensitivity to the surgeon's input. Moreover, the use of brushed motors introduces variability in performance due to inherent brush contact, diminishing the surgeon's ability to execute precise manipulations. In this study, we will primarily focus on improving these limitations to enhance the device's performance.

1.2.2 Mechanical Thrombectomy Phantom Fabrication

In studies that make use of artificial intelligence in autonomous navigation, as of August 2023, 71% carried out evaluations using physical phantoms[11]. In previous works, it is noted that phantoms produced via FDM (Fused Deposition Modelling) perform worse due to the striated texture of the aggregated layers which can interrupt catheter movement [11]. Furthermore, there

appears to be an overall lack of flexibility and compliance in materials that can be 3D printed. There is also a lack of standardised measures to validate the accuracy of anatomical models, which is further exasperated by natural variations in anatomy.

1.2.3 Simulation

To effectively produce a device to carry out mechanical thrombectomy remotely, it is important to be able to simulate the model computationally. Works which explore the simulation of devices such as coils, catheters and guidewires report having issues with accurate geometry modelling regarding the extraction of the actual geometry of the blood vessels due to limitations in spatial resolution, the presence of noise and artefacts [8]. Another major limitation in previous works is the acquisition of in vivo data for biomechanical modelling and haemodynamic simulation. As current imaging techniques lack the resolution capability to provide high-resolution images in space or time, it is difficult to acquire in vivo data including mechanical properties of the vessel wall and rate of blood flow. There is a specific need for faster computation of blood flow and blood-structure interaction for real-time or near real-time simulation.

Across studies, there is a lack of focus on using similar algorithms and extending the experimental environment, slowing progress in the field. Furthermore, several studies keep many variables constant whilst varying another. This poses a challenge regarding the standardization of experimental reference designs for endovascular navigation. The measures for how well an endovascular interventional system performs, vary greatly, worsening the potency of drawing comparisons across studies. Specifically, autonomous and non-autonomous systems do not

appear to be compared using methods that can output meaningful conclusions regarding the benefit of using an autonomous navigation system, with only around 50% of studies making conclusions that consider the integration of an autonomous system [11]. In terms of transferring this research to clinical use, as of August 2023, there are no clinical studies of autonomous endovascular navigation [11].

2 Theory

2.1 Ischaemic Stroke

Stroke is the second most common cause of death globally [12], and fourth most common cause of death in the UK, with a toll of 35,000 deaths annually [13]. Stroke onset is strongly related to age and most likely to occur to those above the age of 55.

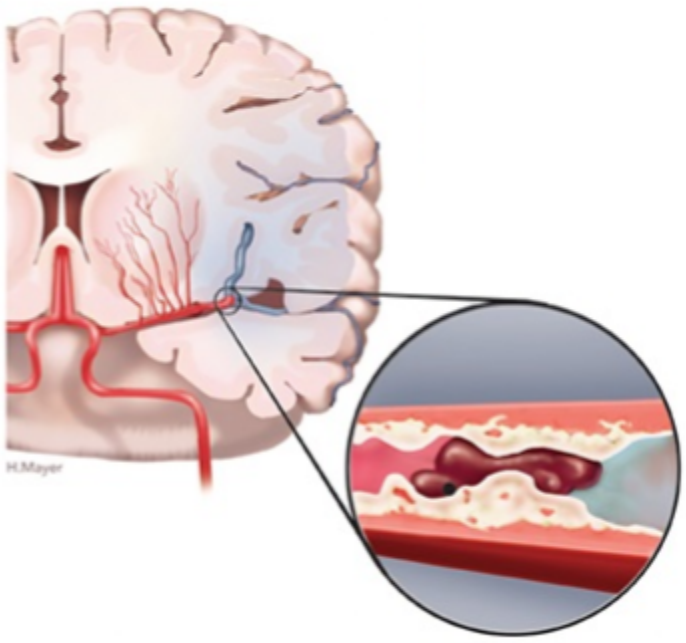

Figure 3: Diagram showing embolism blocking blood flow during ischaemic stroke [14]

Most ischemic strokes occur due to a circulating blood clot which becomes stuck and obstructs blood flow, this occurrence is referred to as an embolism. The most common causes of embolism are large artery atherosclerosis and cardiac conditions like atrial fibrillation. However, there are less common causes such as small vessel disease, which is particularly common in those of East Asian descent [12].

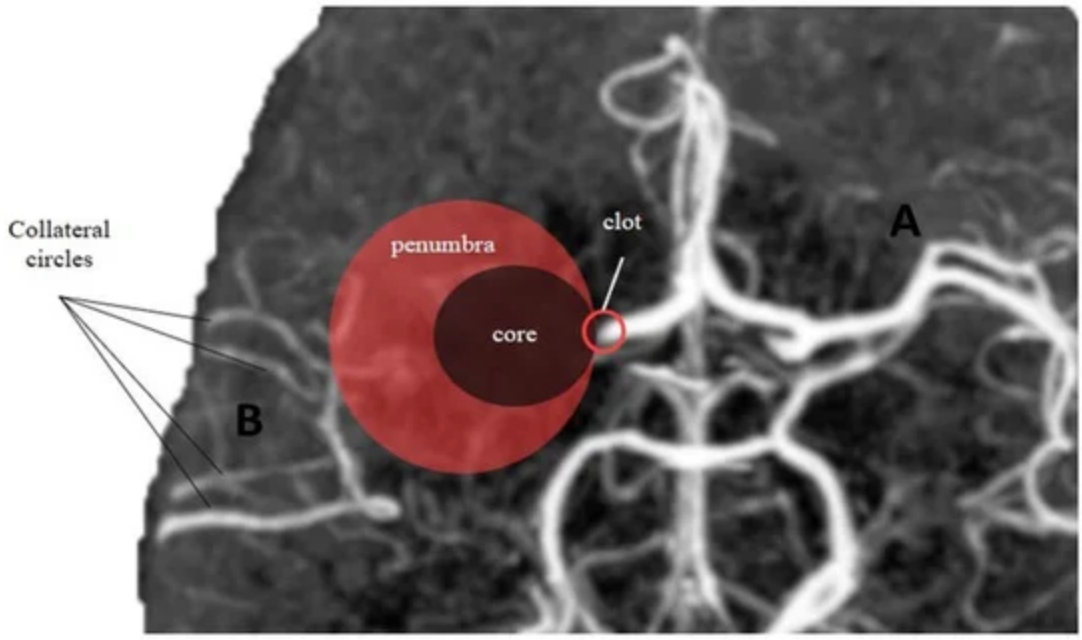

Figure 4: Diagram showing ischemic core and penumbra brain tissue surrounding [15]

Collateral blood flow describes the flow of blood via alternative pathways, this can sustain viability to the injured brain tissue around the area with decreased blood flow. This tissue is referred to as the 'penumbra' and damage to the area is reversible. The penumbra is the target for treatment and it has been shown that around half of ischemic stroke patients show 'penumbra' on MRI.

The immediate effects of ischaemic stroke include arrhythmias, hypertension, a systemic immune response, an increase in cortisol levels, and changes in gut permeability. Furthermore, stroke can cause weakness, partial paralysis, issues with coordination and balance and fatigue [16].

These consequences of ischaemic stroke are mainly attributed to the blockage of a cerebral artery. Reduced cerebral blood flow leads to a decrease in available glucose and oxygen and over time there is the cell death of neurons.

Up to 20% of people suffering from ischaemic stroke respond to intravenous thrombolysis. However, larger clots may not completely dissolve. Other patients may not be able to receive intravenous thrombolysis due to circumstances surrounding previous procedures or prescription medication. Evidence has shown that mechanical thrombectomy is an effective treatment to reduce brain damage and limit, or in some cases prevent long-term disability. Other than intravenous thrombolysis, mechanical thrombectomy brain undergoing necrosis [17].

2.2 Interventional Mechanical Thrombectomy

A mechanical thrombectomy is an interventional procedure by which a blood clot or thrombus is removed endovascularly. The procedure tasks place with image guidance, most commonly X-ray fluoroscopy. It is most often used to treat acute ischemic stroke but can also be used in clot removal for myocardial infarction and pulmonary embolism [18].

There are two main variations of the procedure, relating to the access point, the trans-radial artery (TRA) approach and the transfemoral (TFA) artery approach. Studies show that the TRA approach has a slightly lesser risk of periprocedural complications [19]. Furthermore, the TRA approach allows for a more comfortable recovery process for the patient. However, carrying out

the TRA is slightly more difficult and tends to have a significantly longer procedure time, with average times being 4 hours and 1 hour for TRA and TFA respectively [20].

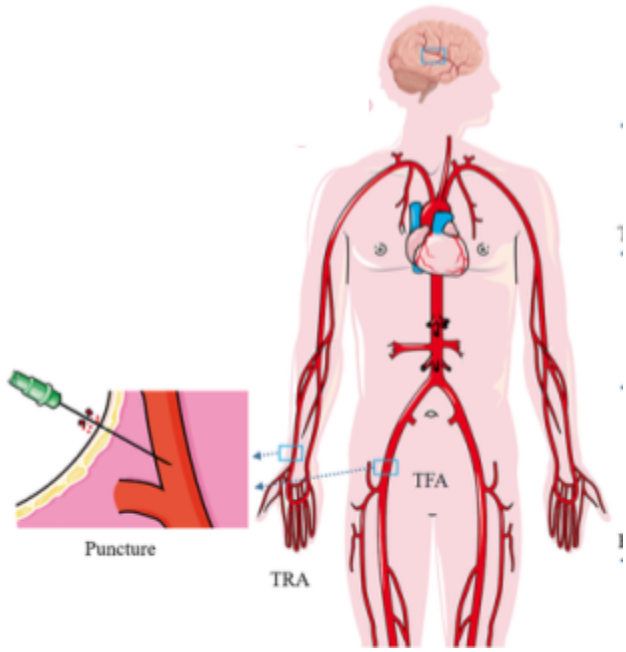

Figure 5: Diagram showing different entry points for mechanical thrombectomy

When accessing the embolism, the catheter passes through the heart. There is significant variation in the structure of the vessels of the heart, specifically the configuration of the aortic arch, which the catheter will pass through. The exact number of aortic arch variations varies between three and five in literature. For the purposes of this project, we will consider the three most common variations of aortic arch anatomy.

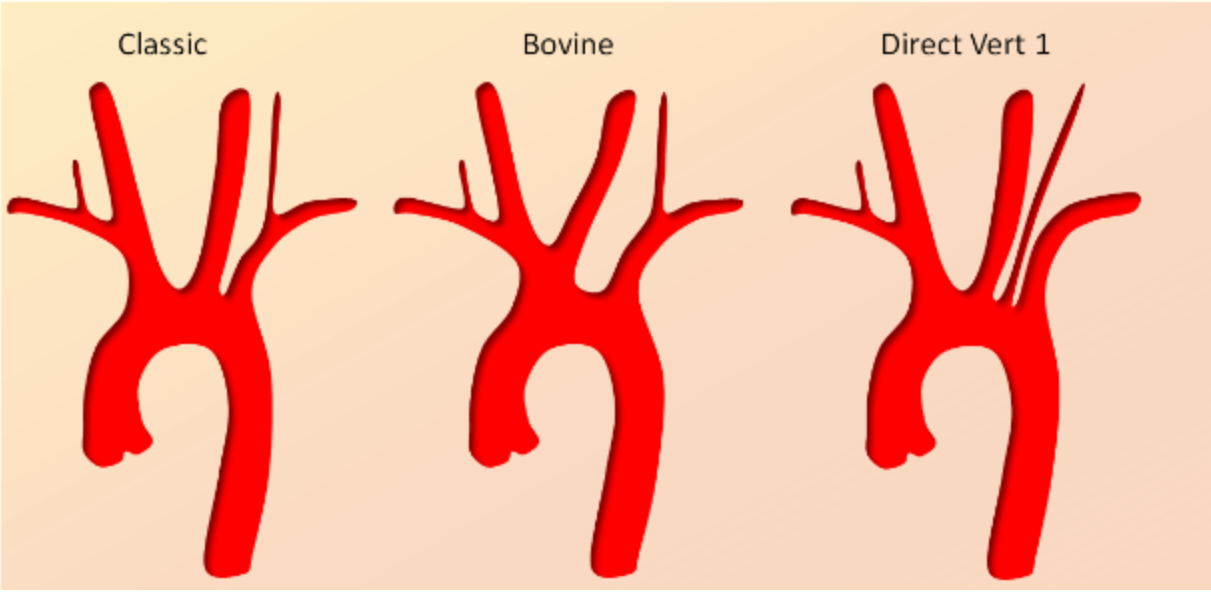

Figure 6: Diagram showing the three most common variations in aortic arch anatomy [14].

A classic arch, is the most common variant and is characterised by three distinct branch vessels given off by the aortic arch; the innominate (brachiocephalic), left common carotid (LCC) and left subclavian arteries (LSA). A bovine arch is characterised by the innominate artery and the LCC artery sharing a common origin [21].

It is important to maintain an awareness of this variation when creating phantoms and training navigational systems.

2.3 Controller responder system

All current endovascular robotic platforms applied to cardiac and peripheral vascular intervention are controller-responder systems [10].

These systems comprise two main components: the controller and the responder. In this report a device-mimicking controller principle was used, which replicates the movement of the surgeon to provide an intuitive control (Figure 7). In contrast, a joystick controller principle is less direct replicas of surgeon's movements. Previous study shows that a device-mimicking controller has an advantage compared to a joystick controller [10].

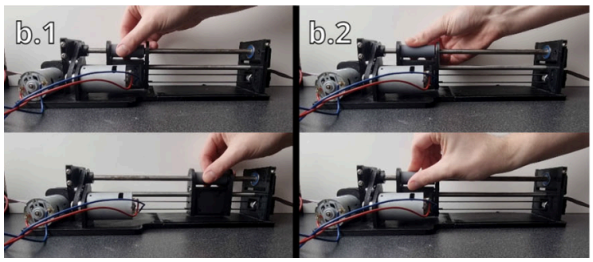

Figure 7: Device-Mimicking Controller operation [10]

The responder executes the commands received from the controller. It manipulates catheters and guidewires with precision, navigating through the vascular system with minimal risk of damage. The exact movements of the responder are crucial for the guidewire to safely travel through vascular pathways, thus playing a pivotal role in the success of thrombectomies.

Robotic controller responder systems can enable precise control of catheters and guidewires. While tele-operated systems allow neurointerventionalists to remotely perform procedures from

any location, as long as patients are near the responder unit. Therefore, a tele-operated robotic thrombectomy system can significantly increase the rate of patient receiving stroke care within less than four hours of the stroke onset [3].

3 Aims

The main aim of this project is to create a toolkit to enable the development of tele-operated techniques for neurointervention, specifically mechanical thrombectomy in treatment of stroke. The primary objectives are :

- Design and manufacture a haptic controller to allow mechanical thrombectomy procedure to be carried out by a clinician remotely.
- Create a reinforcement learning algorithm to assist or independently carry out mechanical thrombectomy procedure
- Create a phantom for the in silico and in vitro testing and training for the algorithm and haptic controller.
- Perform comparative performance studies to show how the toolkit can be used. This includes comparing two different robotic haptic controllers, as well as comparing the reinforcement learning algorithm with that of a human using our robotic haptic controller.

Due to the structure of the project, it has been divided into three sub-projects of which have their own additional secondary aims.

3.1 Haptic Feedback Controller

This haptic controller serves to transition from full simulation to semi-simulation, bridging the gap between virtual simulation and in-vitro experiment. The aim of the haptic controller sub-project is to enhance the design and functionality of an existing controller by integrating linear bearings and brushless motors. This enhancement will optimise the controller's precision and responsiveness in operations. The secondary aim of this sub-project is to use a Plane Scara robot as a substitute control interface to test for the simulation performance.

3.2 Autonomous Navigation

The aim of this sub-project is to create a reinforcement learning algorithm that employs autonomous navigation to assist the mechanical thrombectomy procedure. The algorithm will be developed based on Proximal Policy Optimization (PPO) on Simulation Open Framework Architecture (SOFA). The secondary aim is to analyse the effectiveness of the algorithm and compare it with that of human operation.

3.3 3D Vascular Phantom

The aim of the 3D Vascular phantom sub-project is to develop a flexible 3D-printed vascular phantom that recreates the appropriate anatomy for a mechanical thrombectomy. Furthermore the 3D Vascular Phantom sub-project also aims to investigate methods to simulate synthetic

blood clots and explore the integration of flexible piezoresistive sensors to monitor mechanical feedback.

4 Materials and Methods

4.1 3D Vascular Phantom

4.1.1 3D Slicer

3D slicer is an open-source software package that has applications for several imaging modalities. It can be used for image analysis and scientific visualisation. The ‘SegmentEditorExtraEffects’ extension is an addition to the Segment editor tool. All processes within the extension are semi-automatic segmentation effects which grow segmentations from points defined by the user. The Flood Filling tool, within this extension, works by adding points around the click position to the current segment. Two parameters can be adjusted to inform the intensity tolerance and neighbourhood size.

4.1.2 Segmenting anatomy

Several CT scans including the thorax and head were used to segment blood vessels between the aortic arch and the circle of Willis. The flood-filling tool was used to segment the following vessels. However, several vertebrae and other non-vascular structures were also included in this segmentation.

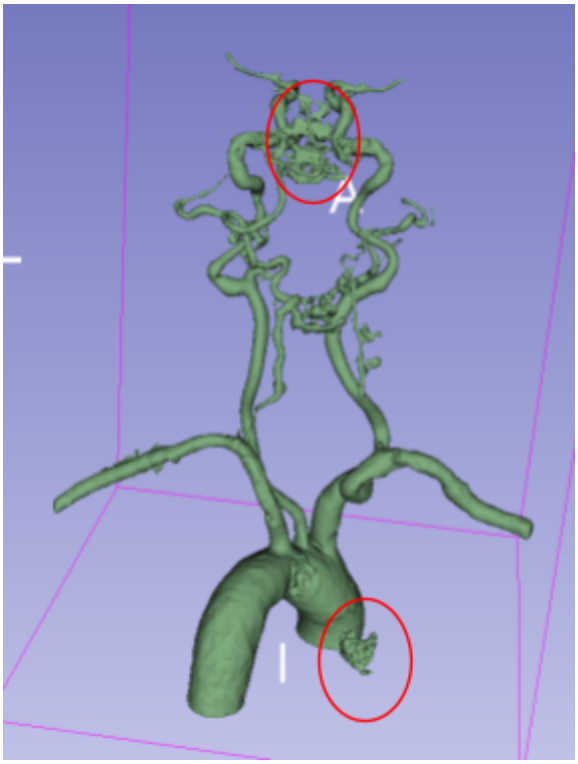

Figure 8: Initial segmentation using the flood filling tool in 3D slicer. Circled in red are vertebrae and lung tissue incorrectly included in the segmentation.

To correct this the ‘Erase’ tool in 3D slicer was used to clean up the segmentation. Following this the ‘Hollow’ tool was used to hollow the segmentation in preparation for printing. 1mm wall thickness was used and the generated object was made using the segmentation's external surface as the new structure's mid-point. The final output spans from the aortic arch to the M1 bifurcation.

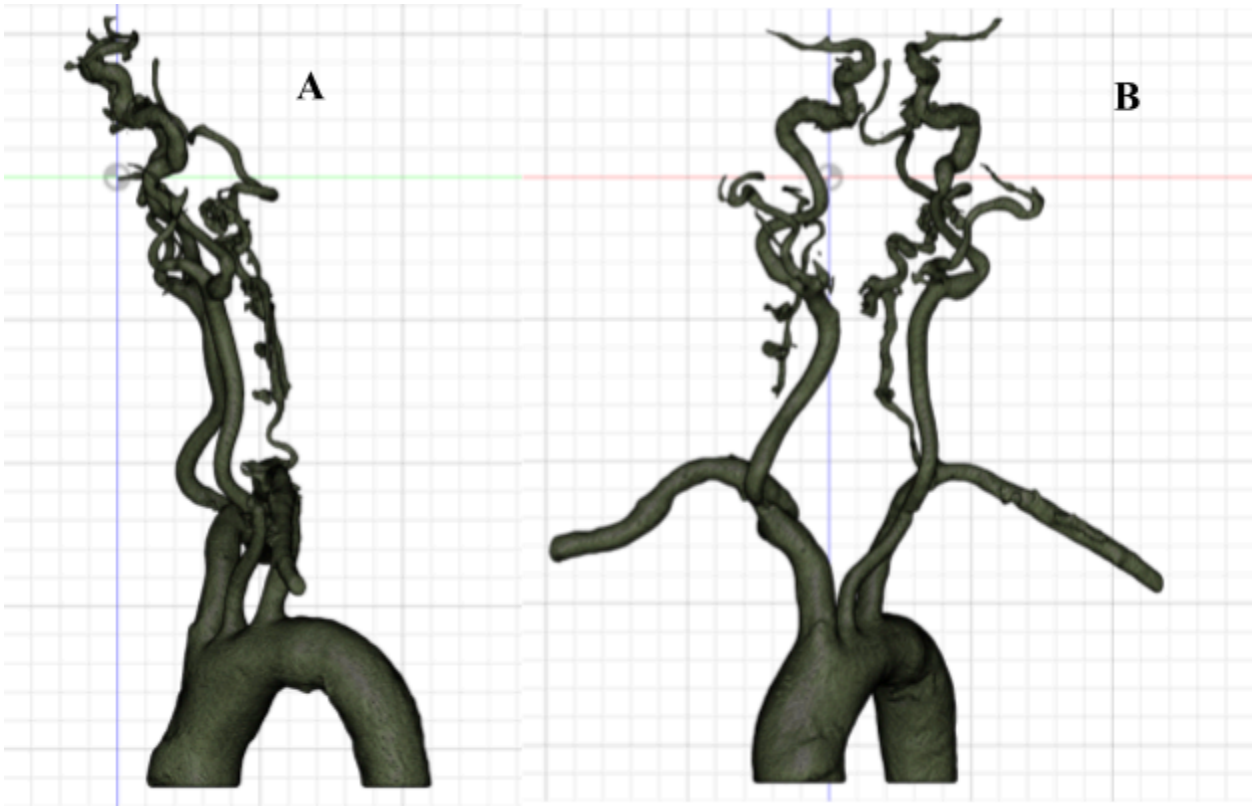

Figure 9: Segmentation with classic arch. A: Sagittal view, B: Coronal view

4.1.3 Materials Testing

To evaluate the suitability of various materials as analogues for vessel walls we carried out mechanical testing on the materials under consideration. Mechanical properties were measured experimentally using tension and stress tests. These tests were carried out using an Instron Machine.

Figure 10: Image of Instron Machine Column

Four samples were tested; Two samples of uncured Sriraya Tech Clear Resin, one sample in a rectangular sheet of 3cm width and 7cm length and the other a lumen of 1cm diameter and 9cm length as well as two samples of FormLabs Elastic 50A resin, one sample in a rectangular sheet of 3cm width and 3cm length and the other a lumen of 1.5cm diameter and 5cm length. All samples were printed at a thickness of 0.5mm. The irregularity of the sample dimensions is a result of the samples being taken directly from phantoms.

Young's Modulus (E) values were calculated using the following equation:

$$E = \frac{FL}{Ax} \qquad \textit{(Equation 1)}$$

Where:

A = Cross-sectional area of the sample (mm^2)

F = Force (N)

x = Extension (mm)

L = Original length of the sample (mm)

4.2 Haptic Controller

4.2.1 Simulation Platform

SOFA (Simulation Open Framework Architecture) is an open-source framework designed for real-time physical simulation. Developed by the French National Institute for Research in Computer Science and Automation (INRIA), SOFA is widely used in various fields, including medical simulation, robotics, and computer graphics.

In this study, the sofa platform is mainly used as a simulation platform to simulate virtual guidewire and virtual vessel tree , and to solve for the guidewire forces according to its collision matrix and stiffness.

This study defines virtual guidewire, virtual catheter and vessel tree based on SOFA platform. The virtual guidewire and catheter are stimulated as a large number of connected 0.5 mm length flexible beams. The tip of the guidewire was set in an inverted J-shape and was made to be able to rotate. Surgeons can target the desired location by changing the rotatory angle of the tip.

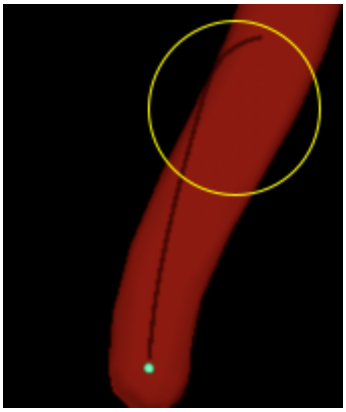

Figure 11: Tip of the guidewire with an inverted J-shape

The tip of the guidewire has a twist radius of 12.1 mm, and a torsion angle of 36 degrees. The hooked part of the tip has a Young's modulus of 12,000 MPa, and the straight part of the tip has a Young's modulus of 80,000 MPa. The outer radius of the guidewire was set as 0.89 mm, while the inner radius of the catheter was set as 1 mm, and the outer radius was set as 1.2 mm.

The aim of this study is to develop an algorithm to aid the navigation in the aortic arch. To obtain more models of the aortic arch, random seeds were used to generate the centerline of the vessels, Left Common Carotid Artery (LCCA), Right Common Carotid Artery (RCCA), Left Subclavian Artery (LSA), Right Subclavian Artery(RSA) and Cardiac Output. Then a vessel tree mesh was generated according to the vessel centerlines point, its radius, and the relative directions of normals at each point.

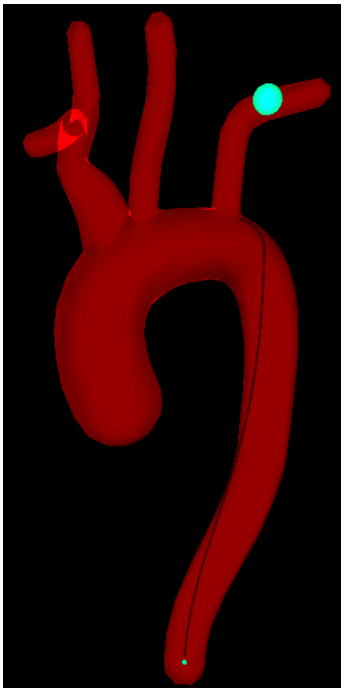

*Figure 12: Visualisation of SOFA(*Simulation Open Framework Architecture*) platform*

SOFA can also simulate the physical interaction between the guidewire and the aortic arch, This enables measurement of the forces on the base and tip of the guidewire, providing data for haptic force-feedback in semi-simulation experiments.

4.2.2 Integration of Linear Bearings in Controller Mechanical Design

According to a survey done in previous work, surgeons have noted that haptic feedback in previous systems often felt unrealistic [10]. This could be partly attributed to the high friction in controller movements. The haptic feedback is relatively small, with the plausible vessel rupture value being 150 mN [10]. Therefore, friction in the controller movement can disrupt the delicate

feedback loop, causing a disconnection between the surgeon's expectations and the actual haptic feedback received. The implementation of linear bearings reduces this friction, thereby smoothing the movement and could potentially enhance the haptic feedback.

The implementation of Bosch Rexroth R0602 [32] linear bearings can significantly reduce friction in carriage's movement along the guide rails. These linear bearings use rolling steel balls, which roll instead of slide, greatly minimising the contract area and friction (Figure 13). The design allows for even load distribution, reducing localised stress and wear.

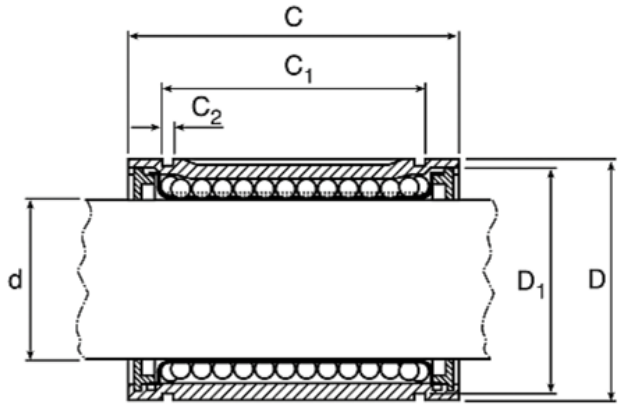

Figure 13: Cross-sectional Diagram of Bosch Rexroth R0602 Linear Ball Bearings [22]

Fusion 360 is a comprehensive 3D CAD tool developed by Autodesk. This project mainly used Fusion 360 for creating and refining the mechanical components.

The guide rails were designed to provide a stable and smooth path for the carriage. The top guide rails feature a slot to engage with the gear connected to the belt, which allows the encoder and

motor to accurately track the carriage's position. The bottom guide rail aligns with the first to ensure the carriage remains perpendicular to the ground, reducing wobble during movement (Figure 14).

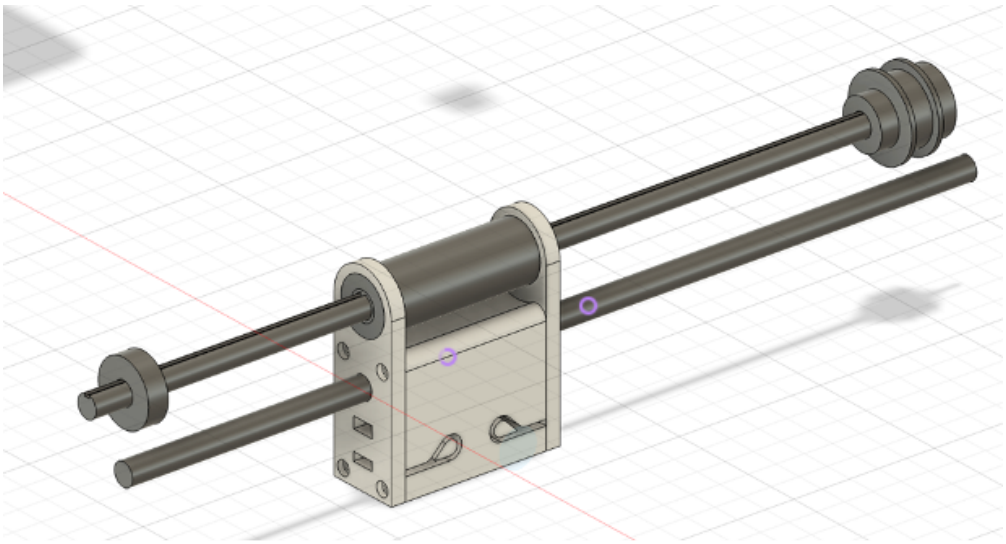

Figure 14: CAD(Computer-aided design) Model of the Guide Rail and Carriage Assembly

The slotted rod used in the design was based on an existing component. This component has developed rust. Unfortunately, due to its unavailability, the rusted rod could not be replaced, this introduces potential limitations and attributes as a source of friction.

Figure 15 shows the CAD design of the carriage to accommodate the linear bearings.

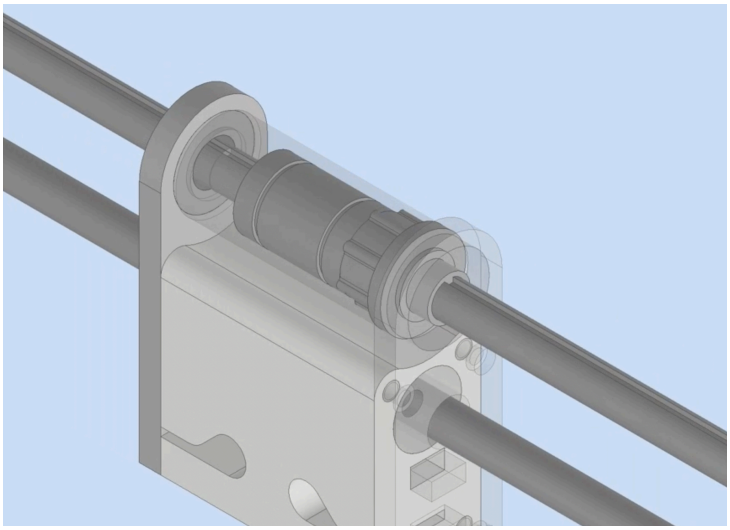

Figure 15: CAD Perspective View of the Carriage Design

The gear (Figure 16) is a critical component to engage with both the slotted guide rail and the linear bearing. It is designed so that the linear bearing fits precisely within it, while its teeth mesh with the slot in the guide rail, allowing for synchronised movement. This component ensures precise tracking of both the carriage's linear and rotational positions, allowing the encoder and motor to monitor and control the carriage's movements accurately.

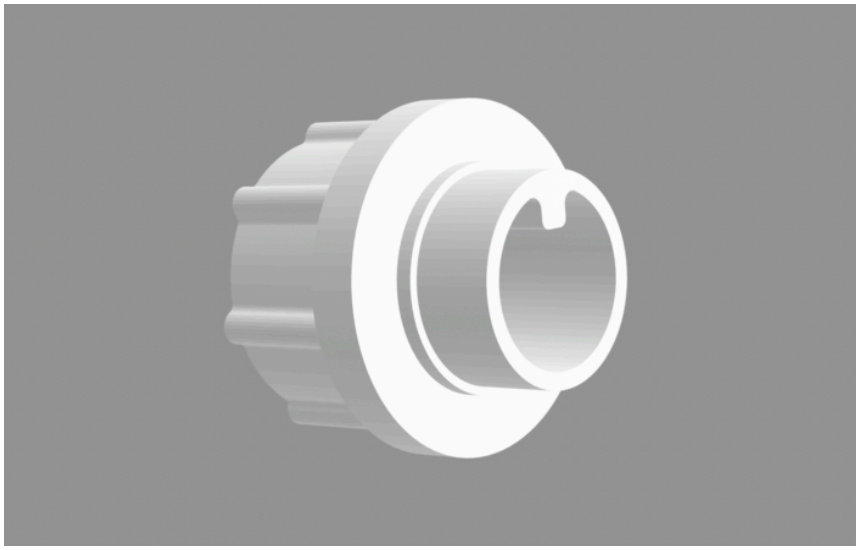

Figure 16: Detailed View of the Gear Design

Following the initial design, modifications were made to reduce friction and stress concentration without changing the bearing model (point 3). The wall thickness at point 1 was reduced, ensuring that the linear ball bearing and the tooth at point 2 are the only two contract points with the slotted shaft. This change minimises friction. Additionally, a rounded edge was introduced at point 2 to reduce stress concentration under load.

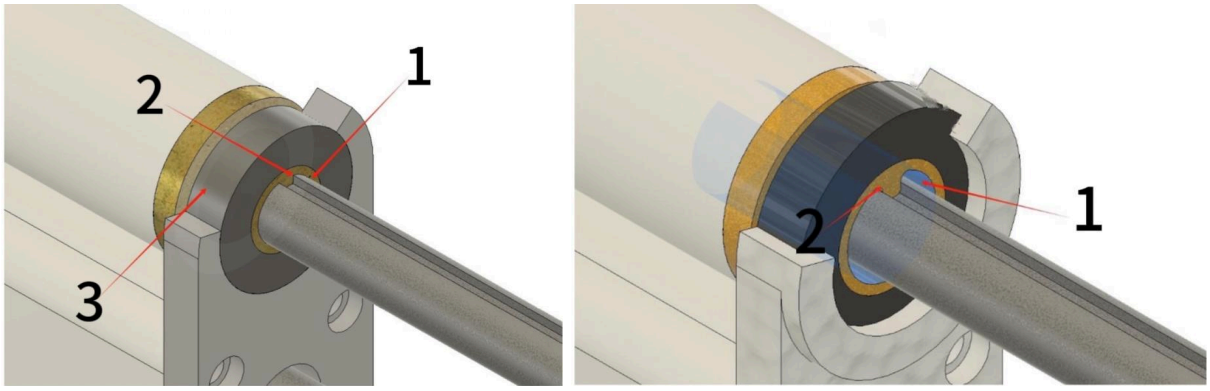

Figure 17: (a) Detailed view before design modifications (b) Detailed view after design modifications

Figure 18 illustrates the steps taken to assemble the redesigned carriage. The components include the carriage body, linear bearings, gears, end plates, and guide rails. The diagram shows the sequential placement and alignment of each part.

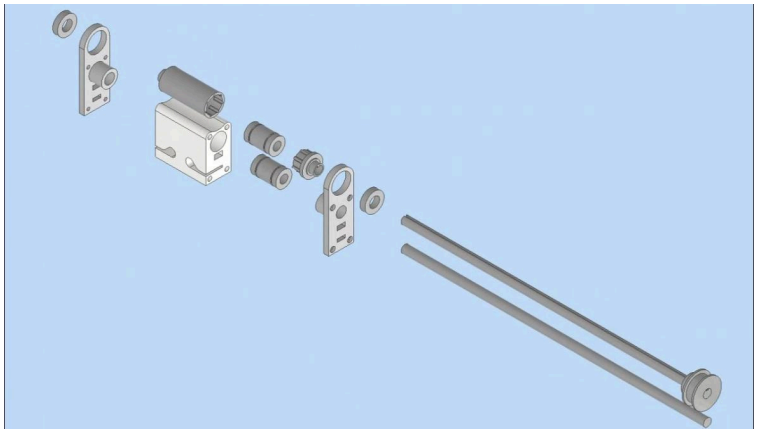

Figure 18: Exploded View of the Redesigned Carriage Assembly

Bambulab X1c is a high-performance 3D Printer designed for complex printing tasks. The carriage body, linear bearings, gears and end plates were all printed using Bambulab X1c.

4.2.3 Integration of Brushless holder in Controller Mechanical Design

In the controller system developed by previous researchers [10], the SOFA simulation environment calculates force feedback based on virtual interactions between the catheter and vessel walls; motors respond to these force signals, simulating the force feedback. The brushed motor in the system is responsible for providing force feedback in both linear and rotatory degrees of freedom (DoF). The first motor provides linear force using a belt pulley system, with an encoder providing real-time position feedback to the controller. The second motors control the rotational movement with a separate belt pulley system, the rotary encoders therefore provide angular position feedback for precise steering. This setup allows for accurate control of the catheter's two degrees of freedom.

Replacing brushed motors with brushless motors addresses multiple drawbacks simultaneously. Brushless motors use electronic commutation control instead of mechanical brushes. As a result, brushless motors can deliver quicker and more accurate feedback during simulations.

The brushless motor used in this project is RS Pro 2163794 model [23]. This model features a 12V voltage supply, a speed of 2910 rpm, and a torque of 0.055 Nm. These specifications ensure that it provides accurate haptic feedback.

The motor holder (Figure 19) is designed to mount the RS Pro 2163794 brushless motor. The holder features a central large hole to accommodate the motor shaft and three surrounding holes

for mounting screws. The shape is optimised to fit within the overall assembly, providing support and reducing vibrations during operation.

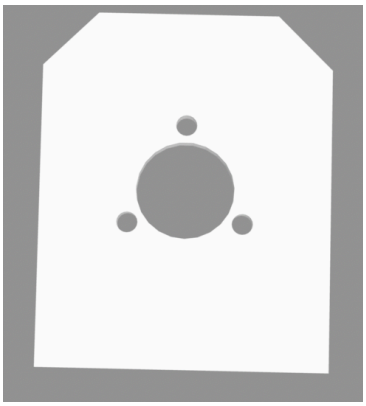

Figure 19: CAD Design of the Motor Holder

The motor holder is also designed to integrate with the belt pulley system. The setup (Figure 20) enables the belt to connect directly to the gear located at the end of the metal rod. This enables the transfer of rotational motion from the motor to the rod, ensures efficient power transmission and precise control.

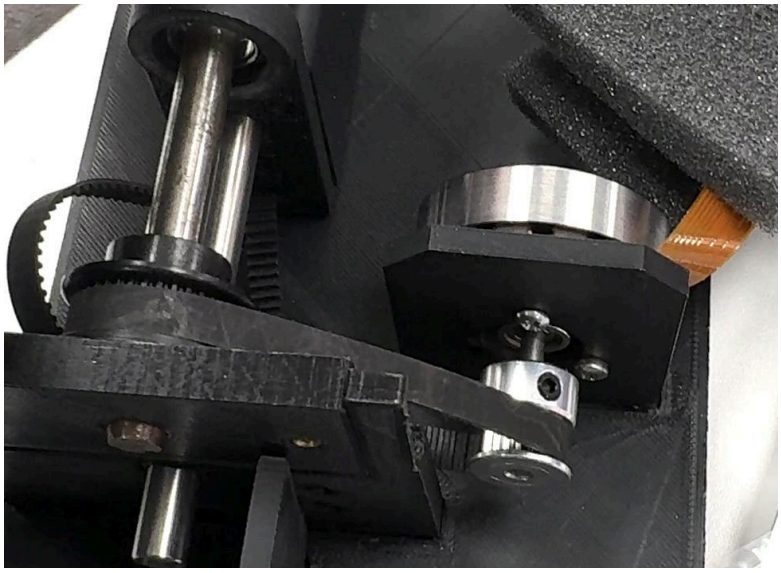

Figure 20: Integration of the Motor Holder with Belt Pulley System

Figure 21 shows the CAD design of the entire controller with integration of the linear bearing and brushless motor. This controller serves as a supplementary material for the project for future semi-stimulation experiments.

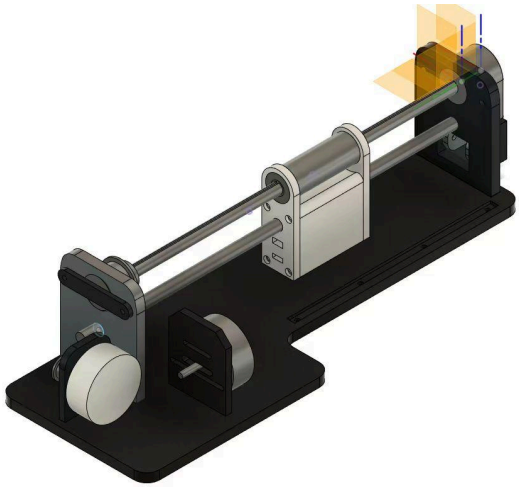

Figure 21: CAD design of the entire controller

Figure 22 shows the assembled controller.

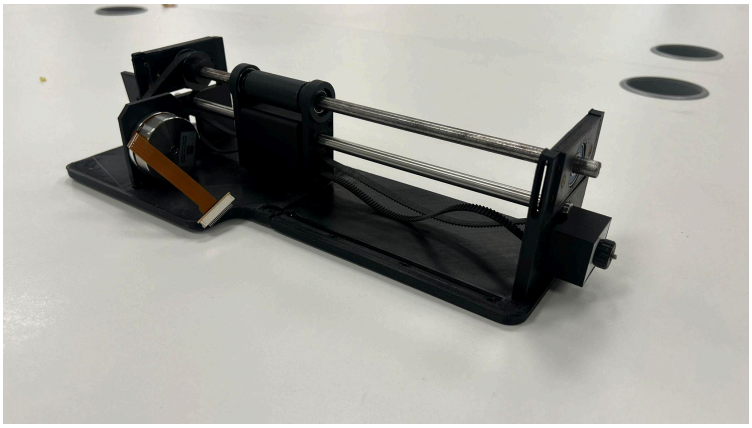

Figure 22: The Assembled Controller

In the latest iteration of the motor holder design, a key improvement allows the motor to be freely positioned before the mounting screws are tightened. This design ensures that the belt tightly engages with the pulley system, reducing the risk of slippage and misalignment. Figure 23 illustrates the motor's adjustable positioning within the holder, from the leftmost to the rightmost positions

Figure 23:(a)Motor Holder Leftmost Position Before Tightening (b)Motor Holder Rightmost Position Before Tightening

4.2.4 Plane Scara robot haptic interface

The Plane Scara robot haptic interface consists of a planar three-link robot, in this setup, the robotic arm can be manipulated by the surgeon to control the virtual guidewire. The robotic arm features three connected rotational joints, each joint being 0.1m in length, and can be driven by a servo motor for rotation. Movements made by the surgeon can be perceived by the encoder embedded in the motor. These movements are then translated into control signals to accurately manipulate the virtual guidewire.

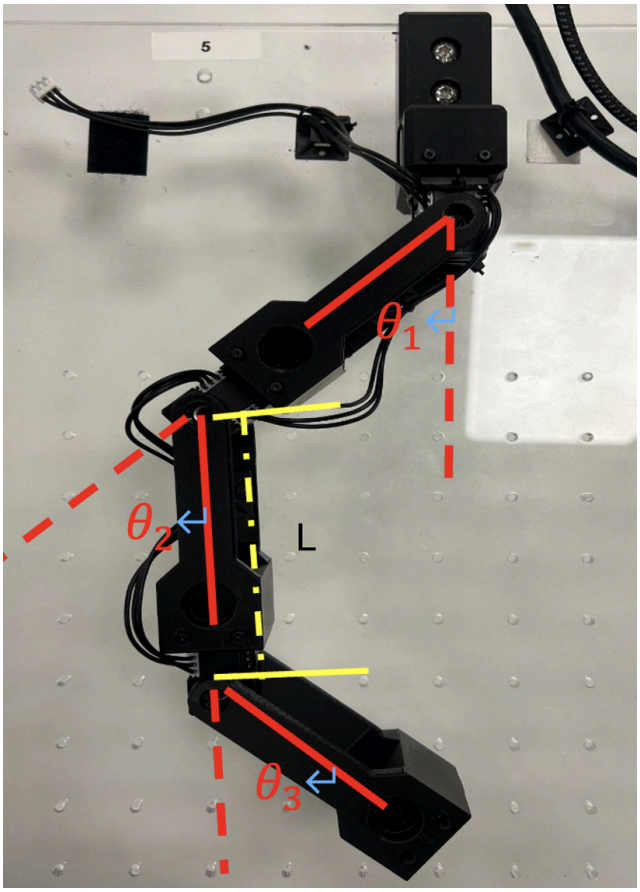

Figure 24: Picture of Plane Scara Robot

The planar three-link robot consists of three links, each rotating around the z-axis, with all links having the same length l. Define the joint angles as θ_1,θ_2,θ_3, then set the base coordinate system at point O_0, and the end positions of each link are denoted as P_1,P_2 P_3.

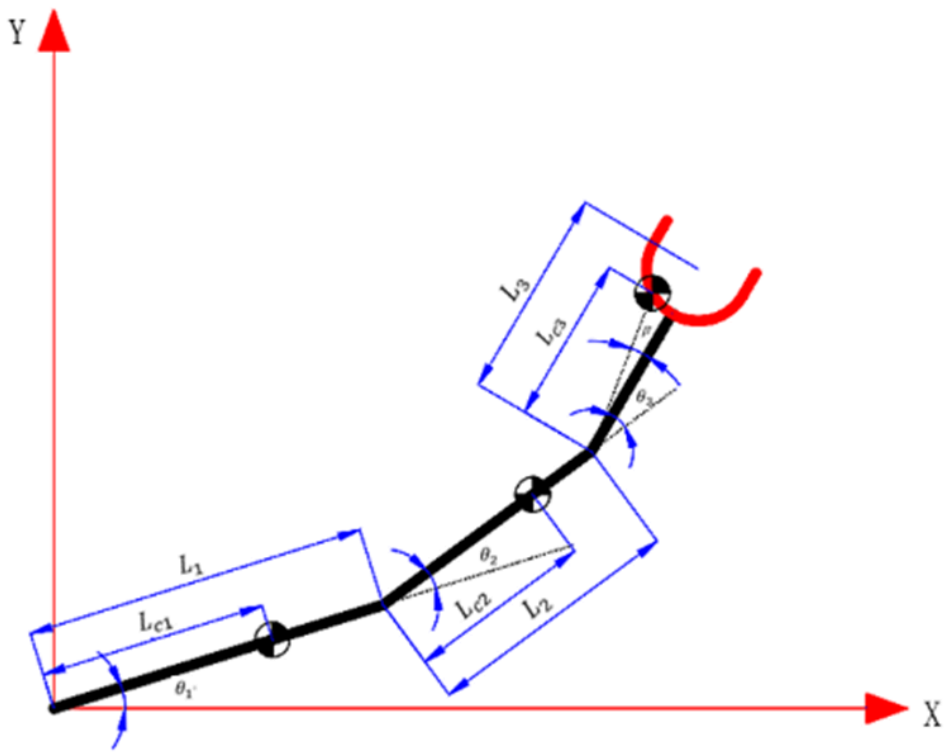

Figure 25: Planar SCARA Robot Kinematics Diagram

The end position of the first link P_1 :

$$P_1 = \begin{bmatrix} x_1 \\ y_1 \end{bmatrix} = \begin{bmatrix} l\cos\theta_1 \\ l\sin\theta_1 \end{bmatrix}$$

The end position of the second link P_2 :

$$P_2 = \begin{bmatrix} x_2 \\ y_2 \end{bmatrix} = \begin{bmatrix} x_1 + l\cos(\theta_1+\theta_2) \\ y_1 + l\sin(\theta_1+\theta_2) \end{bmatrix} = \begin{bmatrix} l\cos\theta_1 + l\cos(\theta_1+\theta_2) \\ l\sin\theta_1 + l\sin(\theta_1+\theta_2) \end{bmatrix}$$

The end position of the second link P_3 :

$$P_3 = \begin{bmatrix} x_3 \\ y_3 \end{bmatrix} = \begin{bmatrix} x_2 + l\cos(\theta_1 + \theta_2 + \theta_3) \\ y_2 + l\sin(\theta_1 + \theta_2 + \theta_3) \end{bmatrix}$$

Therefore, the end-effector position P_3 of the planar three-link robot is determined by the following equation :

$$P_3 = \begin{bmatrix} x_3 \\ y_3 \end{bmatrix} = \begin{bmatrix} l(\cos\theta_1 + \cos(\theta_1 + \theta_2) + \cos(\theta_1 + \theta_2 + \theta_3)) \\ l(\sin\theta_1 + \sin(\theta_1 + \theta_2) + \sin(\theta_1 + \theta_2 + \theta_3)) \end{bmatrix}$$

The Jacobian matrix J is composed of the partial derivatives of the end-effector position P_3 with respect to each joint variable $\theta_1, \theta_2, \theta_3$:

$$\mathbf{J} = \begin{bmatrix} \frac{\partial x_3}{\partial \theta_1} & \frac{\partial x_3}{\partial \theta_2} & \frac{\partial x_3}{\partial \theta_3} \\ \frac{\partial y_3}{\partial \theta_1} & \frac{\partial y_3}{\partial \theta_2} & \frac{\partial y_3}{\partial \theta_3} \end{bmatrix}$$

For x_3:

$$\frac{\partial x_3}{\partial \theta_1} = -l(\sin\theta_1 + \sin(\theta_1 + \theta_2) + \sin(\theta_1 + \theta_2 + \theta_3))$$

$$\frac{\partial x_3}{\partial \theta_2} = -l(\sin(\theta_1 + \theta_2) + \sin(\theta_1 + \theta_2 + \theta_3))$$

$$\frac{\partial x_3}{\partial \theta_3} = -l\sin(\theta_1 + \theta_2 + \theta_3)$$

For y_3 :

$$\frac{\partial y_3}{\partial \theta_1} = l(\cos\theta_1 + \cos(\theta_1 + \theta_2) + \cos(\theta_1 + \theta_2 + \theta_3))$$

$$\frac{\partial y_3}{\partial \theta_2} = l(\cos(\theta_1 + \theta_2) + \cos(\theta_1 + \theta_2 + \theta_3))$$

$$\frac{\partial y_3}{\partial \theta_3} = l\cos(\theta_1 + \theta_2 + \theta_3)$$

Then the Jacobian matrix can be calculated as:

$$\mathcal{J} = \begin{bmatrix} -l(\sin\theta_1 + \sin(\theta_1 + \theta_2) + \sin(\theta_1 + \theta_2 + \theta_3)) & -l(\sin(\theta_1 + \theta_2) + \sin(\theta_1 + \theta_2 + \theta_3)) & -l\sin(\theta_1 + \theta_2 + \theta_3) \\ l(\cos\theta_1 + \cos(\theta_1 + \theta_2) + \cos(\theta_1 + \theta_2 + \theta_3)) & l(\cos(\theta_1 + \theta_2) + \cos(\theta_1 + \theta_2 + \theta_3)) & l\cos(\theta_1 + \theta_2 + \theta_3) \end{bmatrix}$$

Assuming the end-effector needs to apply a force $F = [F_x, F_Y]^T$ as haptic feedback, the relationship between joint torques τ and the end-effector force F can be described using the Jacobian matrix:

$$\boldsymbol{\tau} = \mathbf{J}^T\mathbf{F}$$

Where:

J^T is the transpose of the Jacobian matrix.

$\tau = [\tau_1, \tau_2, \tau_3]^T$ is the torques needed to apply on each joint.

Then, the individual joint torques $\tau 1$, $\tau 2$, $\tau 3$ are:

$$\tau_2 = -l(\sin(\theta_1 + \theta_2) + \sin(\theta_1 + \theta_2 + \theta_3))F_x + l(\cos(\theta_1 + \theta_2) + \cos(\theta_1 + \theta_2 + \theta_3))F_y$$

$$\tau_1 = -l(\sin\theta_1 + \sin(\theta_1 + \theta_2) + \sin(\theta_1 + \theta_2 + \theta_3))F_x + l(\cos\theta_1 + \cos(\theta_1 + \theta_2) + \cos(\theta_1 + \theta_2 + \theta_3))F_y$$

$$\tau_3 = -l\sin(\theta_1 + \theta_2 + \theta_3)F_x + l\cos(\theta_1 + \theta_2 + \theta_3)F_y$$

The first type of manipulation (end-effector controller) offers a way to manipulate the virtual guidewire by controlling only the end-effector of the robotic arm. Figure 26 is an illustration of this control mode. The arm will initially be activated in the default position. The insertion and removal of the guidewire can be controlled by increasing and decreasing the distance between the end-effector and the base coordinate, respectively. The rotational movement of the guidewire can be controlled by adjusting the orientation of the end-effector relative to the base coordinate. In this mode, when the virtual guidewire contacts the vessel wall, SOFA will solve the Z-axis

force at the base of the guidewire and convert it into haptic feedback. The haptic feedback is then applied to the surgeon's hand through the end-effector.

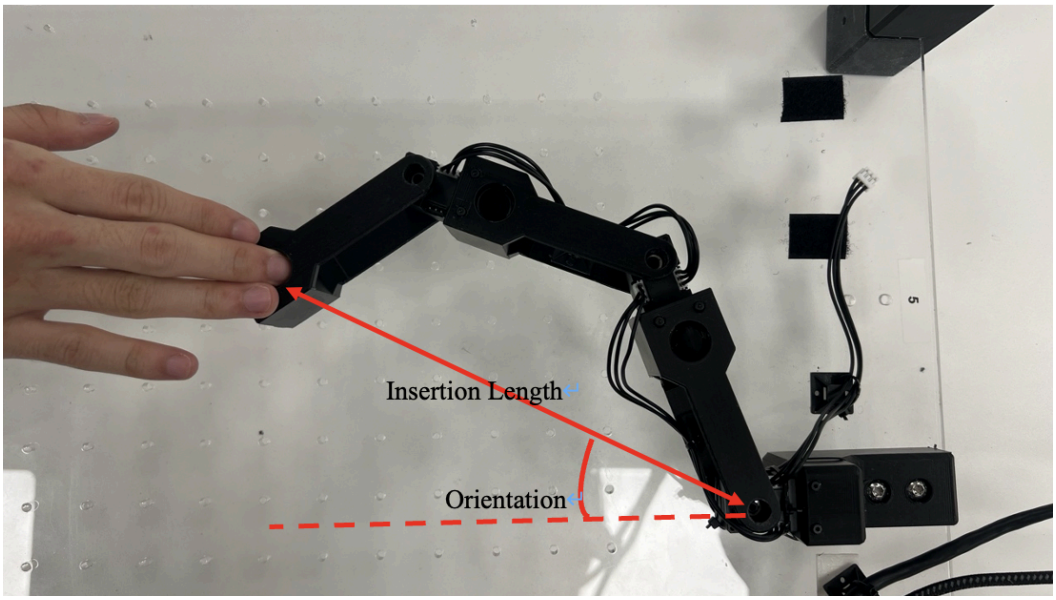

Figure 26:Illustration of end-effector controller

The second type of manipulation offers a way to manipulate the virtual guidewire by controlling the second and third joints (Two-joints controller). Figure 27 is an illustration of this control mode. The arm will initially be activated in the default position. The insertion and removal of the guidewire can be controlled by increasing and decreasing the distance between the second joint and the base coordinate. The rotational movement of the guidewire can be controlled by rotating the third joint. In this mode, haptic feedback will be applied to the surgeon through the second joint, not the third, to avoid any unintentional rotational movements.

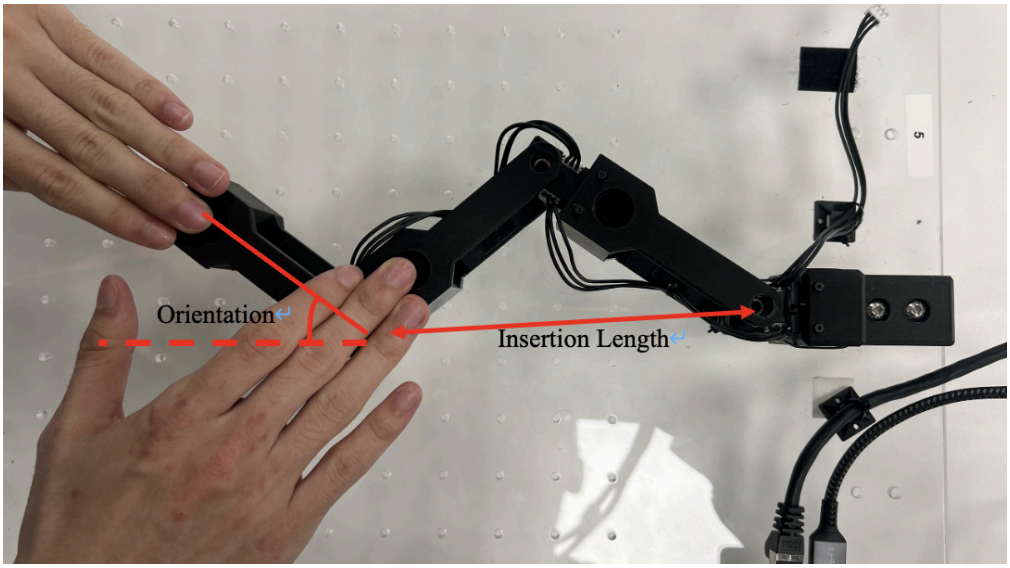

Figure 27: Illustration of two joints controller

4.2.5 Example of Plane SCARA Robot being used for an experiment: Performance Comparison of Controller

To illustrate the practical application of the haptic interface designed in this project, a semi-simulation experiment was conducted. In this experiment, the robotic arm was connected to a PC via UDP socket. This configuration allowed the surgeon to control a virtual guidewire displayed on the PC by manipulating the robotic arm. The experiment was designed to evaluate the responsiveness and accuracy of the haptic feedback provided by the system in real-time during neurointerventional procedures. This setup not only tests the functionality of our toolkit

but also provides critical data on the efficacy of different haptic controllers under simulated clinical conditions.

At the start of the experiment, the system developer introduced the participants to the control modes of the robotic arm. Then, each participant was given 5 minutes of free time to interact with and familiarise themselves with the SOFA system. Participants were required to use the two distinct control modes(end-effector controller and two-joints controller) to drive the virtual guidewire towards a specified target located within each branch. These branches included the Right Common Carotid Artery, the Left Common Carotid Artery and the Left Subclavian Artery.

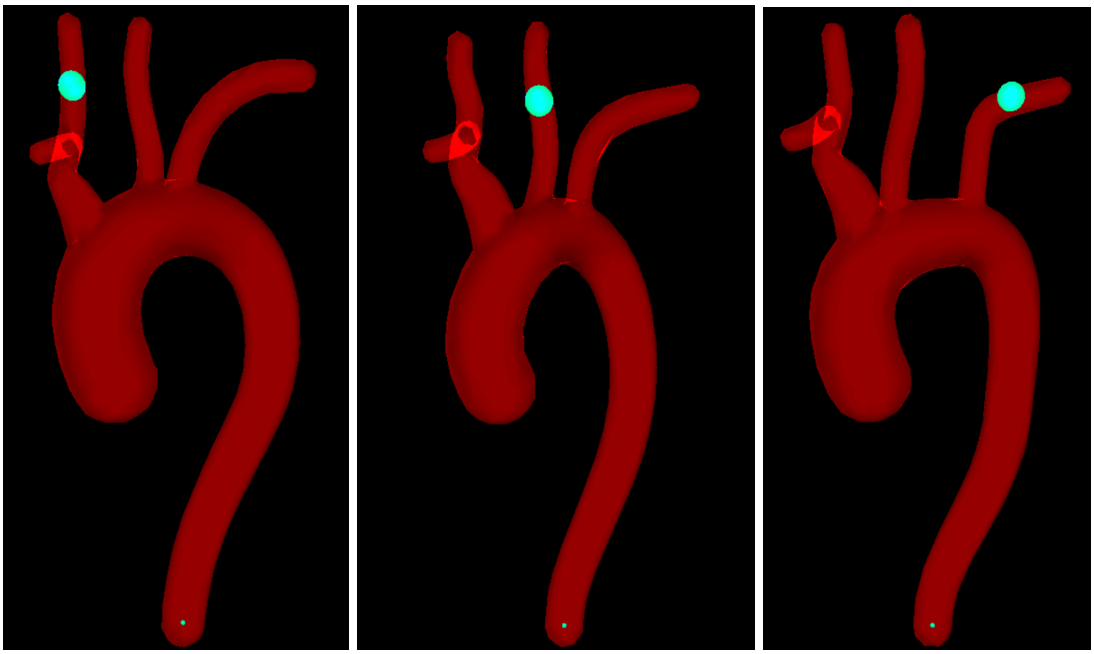

Figure 28: Target in the Right Common Carotid Artery, the Left Common Carotid Artery and the Left Subclavian Artery

When the guidewire tip reached the target point, SOFA recorded the total navigation time spent by the participant, as well as the maximum force applied to the guidewire tip and base during navigation. At the end of the experiment, the participant was asked to finish a questionnaire. The questionnaire collects their feedback from several perspectives including the realism of the guidewire movement, the anatomical accuracy of the stimulation, and the effectiveness of the haptic feedback. Experiments were carried out among 3 inexperienced participants, 1 experienced participant and 1 clinician. The results were shown in 5.2.

4.3 Autonomous Navigation

4.3.1 Virtual thrombectomy environment.

This session explains the key module used for development of autonomous navigation algorithm.

The Intervention module is the basis of the whole simulation design. It is designed to enhance the accuracy and reliability of medical intervention through several basic functions such as force sensing and robot motion control in simulated environments.

The force sensing module aims to monitor and calculate tip forces, base forces and torques during the intervention. The calculations are based on data from the collision detectors and the stiffness parameters of the springs positioned at the bottom of the guidewire. These calculations

help to understand the stress exerted on the guidewire and thus provide basic data for force feedback control.

The SOFA core module is used to add and manage various components to the simulation, ensuring that objects in the simulation are displayed and interact correctly.

The target module is mainly used for target management and localisation in the robot simulation system. The virtual thrombus, as a target for navigation, will be set in a defined vascular branch with specific locations by random seeds. SOFA records the distance between the target and the guidewire tip, then returns a completion flag to reinforcement learning after the guidewire tip reaches the target.

The vessel tree module is mainly used to simulate the vessel tree structure. These modules include several vascular structures for robot simulation and medical interventions by defining vascular branches, generating random vascular trees, and importing vascular trees from grids.

The device module is mainly used to set up the guidewire and catheter we used. The physical properties of the virtual guidewire were set in advance, including guidewire diameter, maximum inserted length, degree of tip bending, tip bending radius, Young's modulus of the guidewire, as well as mass, friction and other properties.

The fluoroscopy module is mainly used to simulate and process X-ray image data which is important for navigation and localisation of robots in vessels. The module provides detailed fluoroscopy image processing functionality through defining image properties, transforming coordinate systems and generating simulated images.

The observation class is designed as a base class for different types of observational data collected during intervention. The system is designed to observe multiple data elements such as relative insertion lengths, device lengths, target coordinates and tracking points for comprehensive intervention monitoring and analysis.

Throughout the design of the pathfinder system, Pathfinder defines the basic interfaces and properties required by the path planner. The main properties include path length, 3D path points and their corresponding 2D transformations etc. A breadth-first search (BFS) algorithm is used for path planning in the actual implementation.

In the design of the reward function, several reward components are defined: a goal reward, a path length change reward, and a step penalty. Among them, the target reward will have a larger reward value when the robot reaches the goal, and this reward is designed so that the robot can obtain a significant reward increase when approaching the goal.

During the training process, the robot continuously approaches the goal by executing actions, and the path length change and step penalties at each step enable the robot to optimise the path in

a stable and fast manner. However, when the robot finally reaches the goal, a goal reward is triggered, which is significantly higher than the normal step reward, thus reflecting an exponential increase in reward to motivate the robot to optimise its behaviour to reach the goal as quickly as possible. In this way, the robot gradually learns the optimal operation strategy and achieves effective task completion through multiple cycles and experience accumulation during the training process.

4.3.2 Proximal policy optimization reinforcement learning.

Reinforcement learning involves an agent learning to make decisions through interactions with an environment, with the objective of maximising cumulative rewards over time [31]. There are two objects that can be interacted with in reinforcement learning: Agent and Environment:
Agents can sense the state of the environment and, based on the feedback rewards, select an appropriate action to maximise the total long-term gain. The Environment receives a series of actions performed by the agent, evaluates the series of actions and converts them into a quantifiable signal for feedback to the Intelligence.

Proximal Policy Optimization (PPO) is a reinforcement learning algorithm designed to improve policy gradient methods by ensuring more stable and reliable training. PPO balances exploration and exploitation by iteratively updating policies using a clipped objective function [30] that prevents large updates, thus maintaining proximity to the current policy. PPO updates the policy

by sampling from the environment, calculating gradients, and adjusting the policy within a trust region to avoid drastic changes. This method enhances learning stability and efficiency.

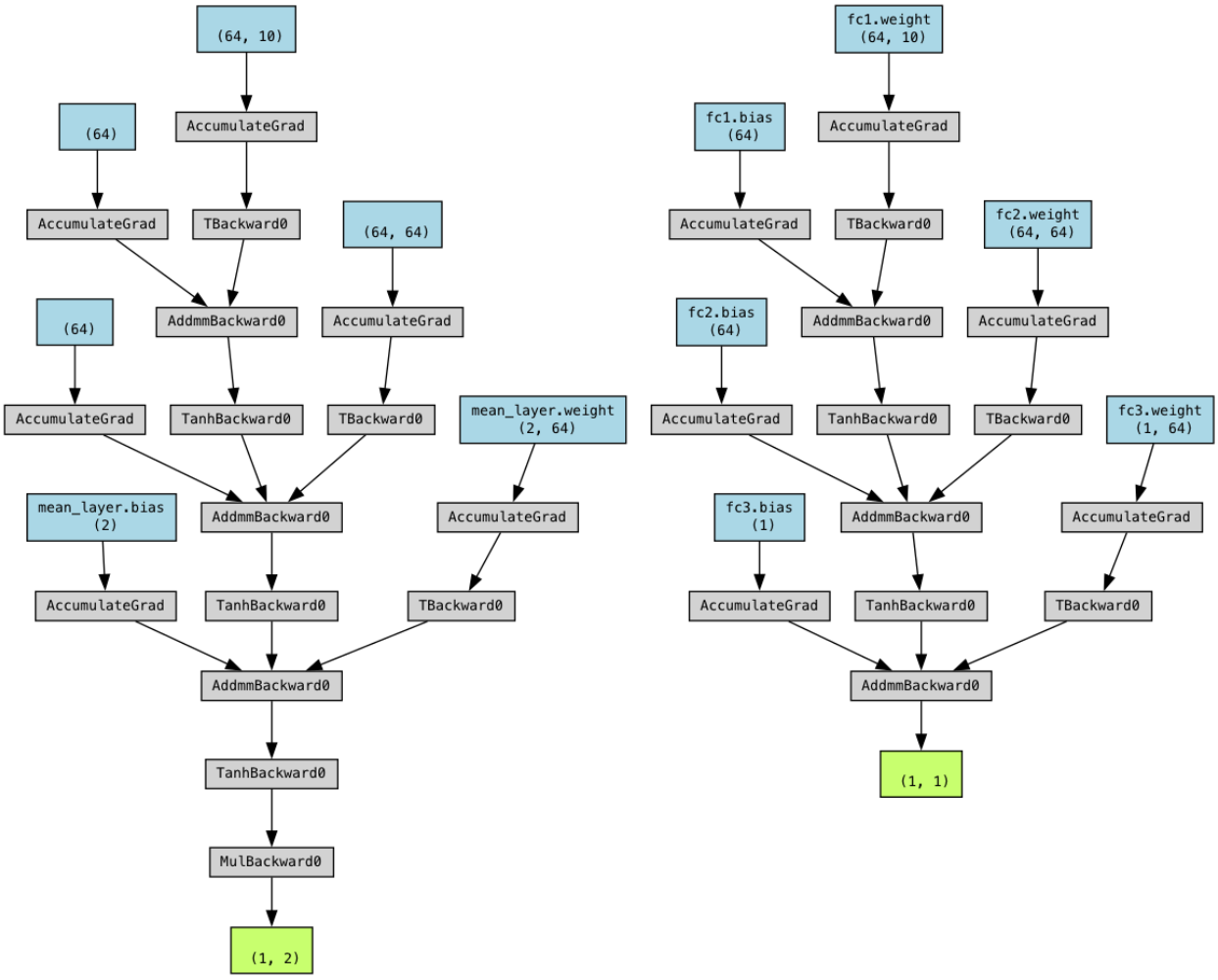

Figure 29: Reinforcement Learning Network Structure

Proximal policy optimization is suitable for autonomous navigation in intravascular environments due to its robustness and stability in high-dimensional space. Due to the

complexity and dynamics of blood vessels, accurate and reliable decision-making is essential. PPO can improve the safety of intravascular navigation by ensuring stable training using a truncated objective function that prevents excessive updates. In addition, the PPO algorithm is good at processing continuous action space, which makes it more efficient in dealing with vascular environments.

4.3.3 Training strategies for autonomous navigation.

With navigation as a goal, the design of the reward function is significant to the efficiency of training and the ability to complete the navigation. Typically, the reward function consists of a constant time penalty term and a large reward for eventually navigating to the goal. However, navigating a guidewire within the aortic arch is different from regular training scenarios as the vessel wall acts as a spatial constraint with a more complex structure and interaction with the guidewire. Curriculum strategies were designed to effectively enhance training efficiency and navigation success. The path from the inserted position to the target position was segmented into 14 equal parts (shown in Figure 30), and each segmentation point was set with a subtarget, with each subtarget having a much smaller reward than the final target. As the reinforcement learning model learns in the aortic arch, it will receive small rewards after reaching these sub-targets, which motivate the system to continue exploring on the correct path.

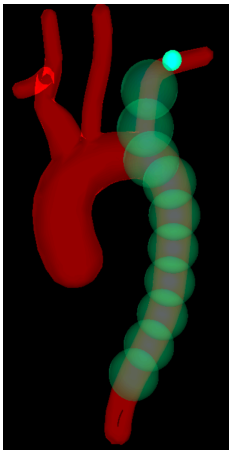

Figure 30: The path to the target position was segmented into 14 equal parts

While using curriculum learning, an exponential growth mechanism was added to the reward function in order to accommodate the complex structure of the vascular branches at the entrance in the aortic arch, a mechanism that will adjust the weight of the rewards obtained. During autonomous navigation, the closer you get to the target, the reward for each success in reaching the subtarget increases exponentially, which gives a smooth curve to the rewards gained from reinforcement learning and places more emphasis on navigation under complex structures as the guidewire approaches the target.

The entropy term is designed as part of the strategy's loss function, which encourages the strategy to maintain randomness in its choice of actions by calculating the entropy value of the current strategy (dist_entropy) and adding a negative entropy value multiplied by a factor (self.entropy_coef * dist_entropy) to the loss function. This mechanism ensures that the strategy

maintains a certain level of exploration during training, avoids premature convergence to suboptimal solutions, and promotes the strategy's search for optimal solutions in a larger state space.

4.4 Synthetic Clots

In recreating the anatomy of an embolic stroke, it is important to represent the embolism itself. By creating an analogue for the clot it allows for consistency in the size, shape and composition of clots. Hence, creating a controlled environment from which to draw research findings, allowing findings to be more reproducible and reliable. Furthermore creating clots from synthetic materials circumvents issues regarding the use of animal substitutes. Within this study, synthetic clots will be placed into the phantom.

Types of Clots

Research shows that the composition of blood clots can have significant effects on the characterisation of ischemic stroke. The composition of the clot depends greatly on the origin of the clot. Thrombi can be approximately divided into two groups, venous and arterial. Venous thrombi are composed of mainly entrapped blood cells within a fibrin structure. This gives venous clots a red appearance. Arterial thrombi usually develop when platelets adhere to the injured vessel wall over abnormal accumulations of fats, cholesterol, cellular waste, and other substances, known as atherosclerotic lesions. Arterial thrombi are usually described as ‘white’ clots. This distinction also influences the most suitable treatment. Venous clots are treated with anticoagulants, and arterial clots are treated with antiplatelets. Despite this categorisation, the

majority of strokes do not fit perfectly into one of these two categories. Different stroke etiologies also have distinct variations in thrombus composition:

Stroke Etiology	**Thrombus composition**
Cardioembolism	● Higher red blood cell proportions ● High T cell number
Large-artery atherothrombosis	● Low red blood cell proportions ● High level of fibrin and platelets ● High white blood cell proportions

Table 1: Different thrombus composition depending on the cause of the occlusion.

4.5 Statistical Method

In the comparative analysis of our study, T-tests were employed to assess the significance of differences observed between data.

All statistical tests were conducted using MATLAB. A standard significance level of 5% was used to determine statistically significant differences. In cases where P-values were between 0.05 and 0.1, results were considered to exhibit a trend towards significance, suggesting a potential relationship that may require further investigation to confirm.

5 Results

5.1 3D Vascular Mesh

Figure 31 shows the centreline and mesh pulled from an anonymized CT scan. The mesh includes anatomy from the inferior section of the aortic arch to the Circle of Willis. Detailed methodology regarding the segmentation process is provided in section 4.1.6. The centreline was obtained using the SlicerVMTK module in 3D Slicer. Visualisation of the extracted points was computed using custom Python script.

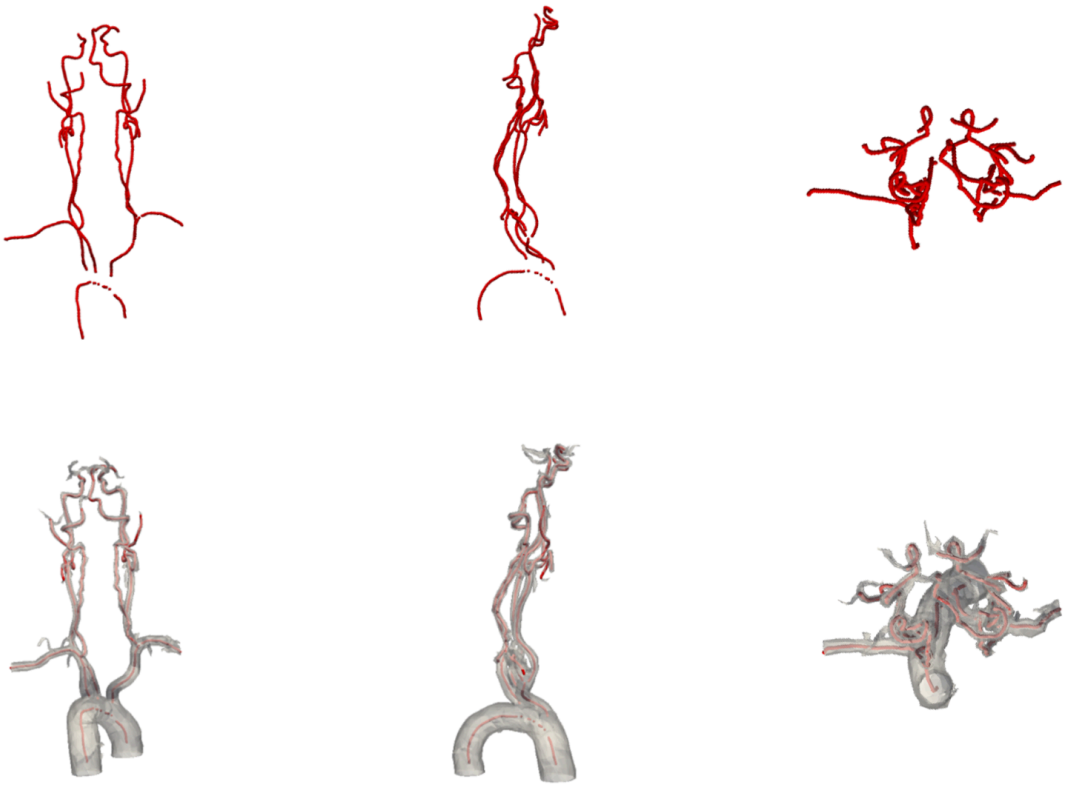

Figure 31: Centreline and mesh of custom segmentation pulled from anonymized CT data.

5.2 Haptic Interface

5.2.1 Experimental design

Detailed experimental method was documented in 4.2.5. As mentioned, the semi-simulation experiments were designed to demonstrate the use of the toolkit and to evaluate the haptic interface. The experiments were conducted as bench tests.

A stepwise approach was taken for the experiment. In the initial phase of the experiment, the participants included 3 Masters students, which for the purposes of this study will be referred to as 'Inexperienced Users' as well as the supervisor who had some clinical experience, who for the purposes of this study will be referred to as an 'Experienced User'. The results of the experiments were shown in 5.2.2 and 5.2.3. In later stages of the experimentation, a clinician was also incorporated to provide a more comprehensive evaluation of the haptic interface. The results were shown in 5.4.

Figure 32 shows the overall setup of the system and a participant. Details of this setup can be found in section 4.2.4. Shown in Figure 32 is the PC hosting the SOFA simulation environment and the attached Plane Scara robotic arm used for control.

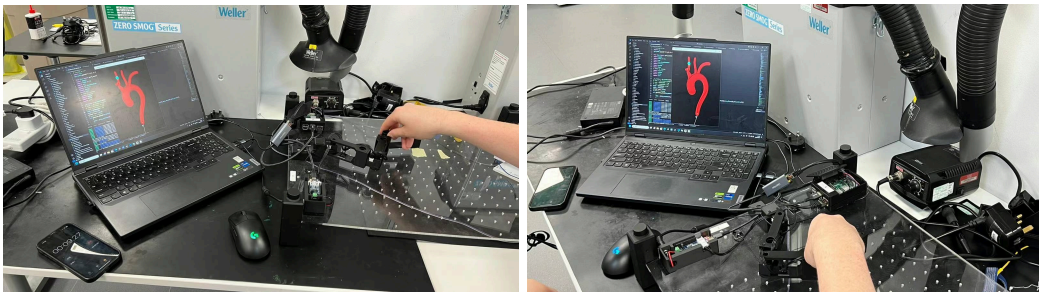

Figure 32: Overview of haptic interface and robotics arm interface

5.2.2 Navigation time: Performance Comparison

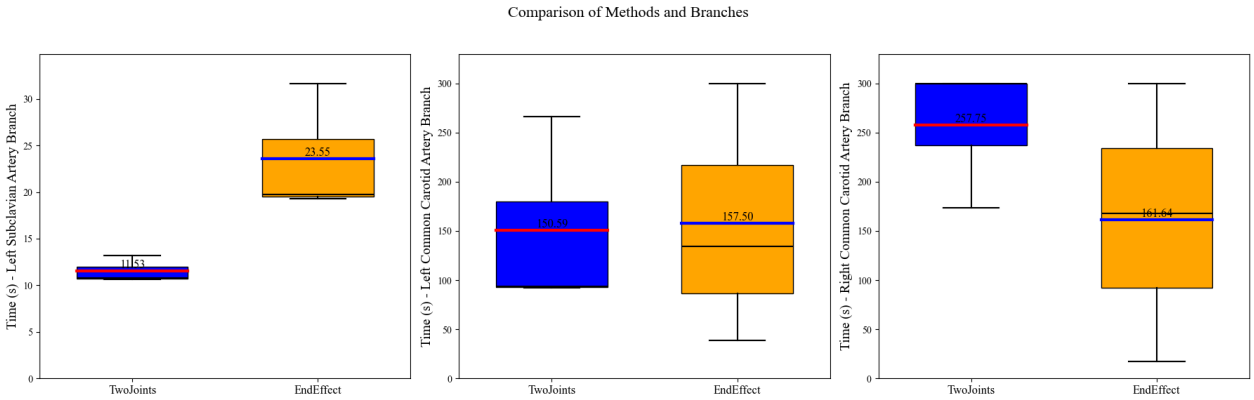

Figure 33: Time For Inexperienced Users reaching target of different branches

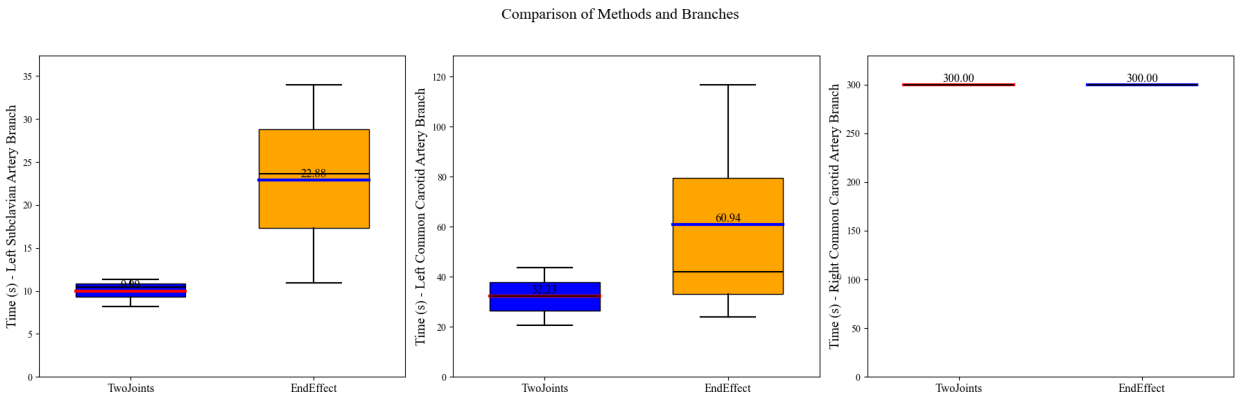

Figure 34: Time For Experienced Users reaching target of different branches

		Mean Time (s)		
Controller	Participants	Left Subclavian Artery	Left Common Carotid Artery	Right Common Carotid Artery
Two Joints	Students	11.53	150.59	257.75
	Experienced Users	9.99	32.23	300
End Effect	Students	23.55	157.5	161.64
	Experienced Users	22.88	60.94	300

Table 2: Mean Navigation Time Data by human operation

Figures 33 to 39 are box plots, in these plots, the bands inside the boxes represent the median values of the data, while the top and bottom edges of the boxes indicate the interquartile range (IQR). IQR shows where the middle 50% of data points lie. The lines extending from the boxes, known as "whiskers", illustrate the upper and lower extreme of the data. The black lines show the median of the data, the red and blue lines show the average value of the data

Figures 33 and 34 show the average completion times for the Inexperienced and Experienced users respectively to navigate to the LSA, LCCA and RCCA. For the purposes of analysis, when a user failed to complete the task within the allotted time, the time was recorded as 300 seconds. For the navigation time of the LSA (Left Subclavian Artery) and LCCA(Left Common Carotid Artery), the Two Joints controller was less on average than the End Effect method ($P = 0.6436$). However when navigating the RCCA(Right Common Carotid Artery), the End Effect controller performed better ($P = 0.3802$).

It is observed that the experienced users utilise less time to perform navigation tasks in LCCA and LSA branches, which to some extent suggests that experts with prior knowledge can adapt to the machine faster. However, the navigation time for students in the RCCA navigation task was less, this is likely due to students being more familiar with the design of the system as developers.

The navigation time took and the fail rate in the RCCA branch were the highest during the task. One of the reasons could be due to the limitations introduced by simulation. During simulation, 3D structures were projected into a 2D image, which limits participants' ability to obtain spatial information particularly at the right subclavian artery intersecting RCCA. The intersection of RCCA with the right subclavian artery is shown in figure 35.

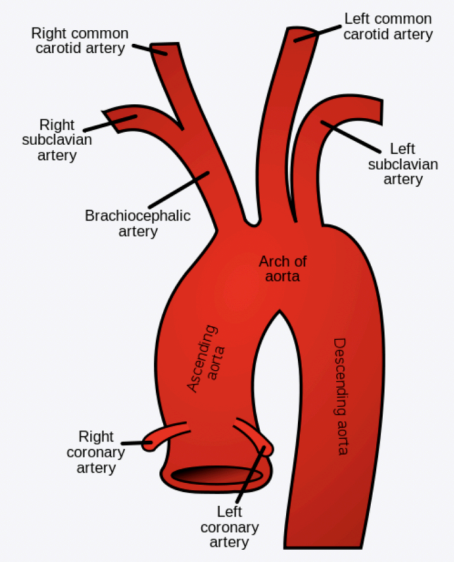

Figure 35: Right subclavian artery intersecting RCCA(Right Common Carotid Artery)

5.2.3 Force Analysis: Performance Comparison

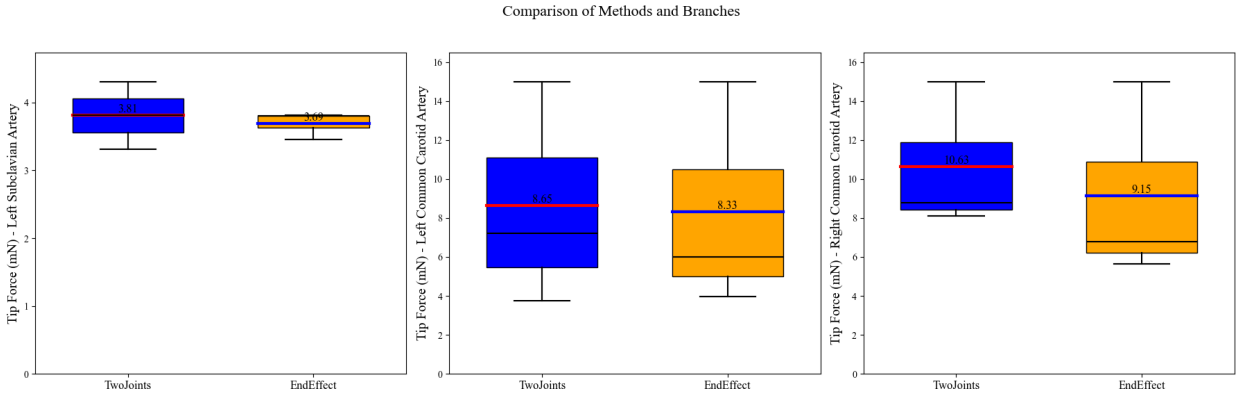

Figure 36: Tip Force from inexperienced user

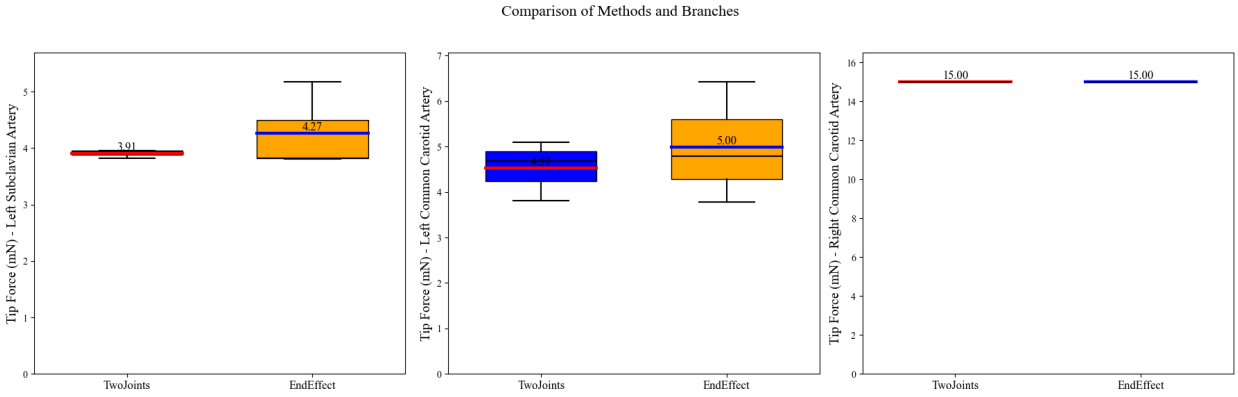

Figure 37: Tip force from experienced users

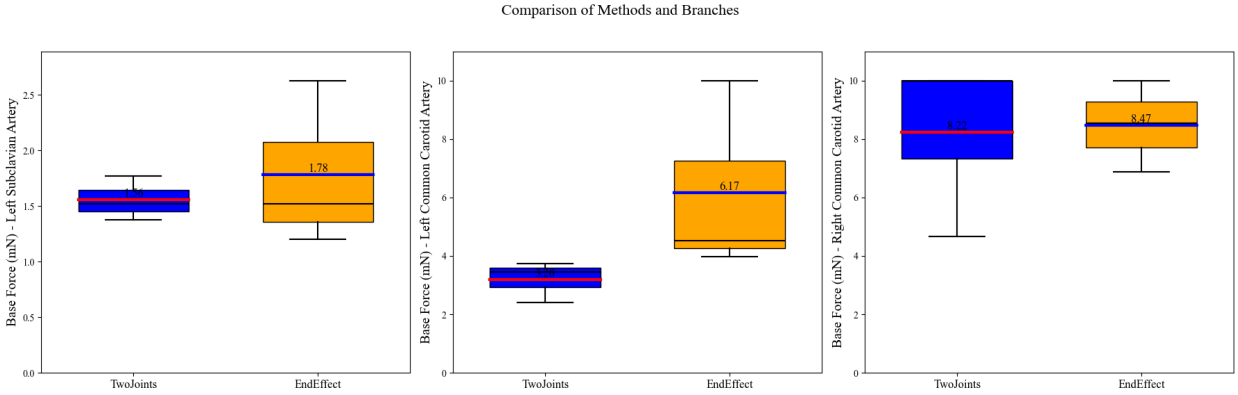

Figure 38: Base force from inexperienced user

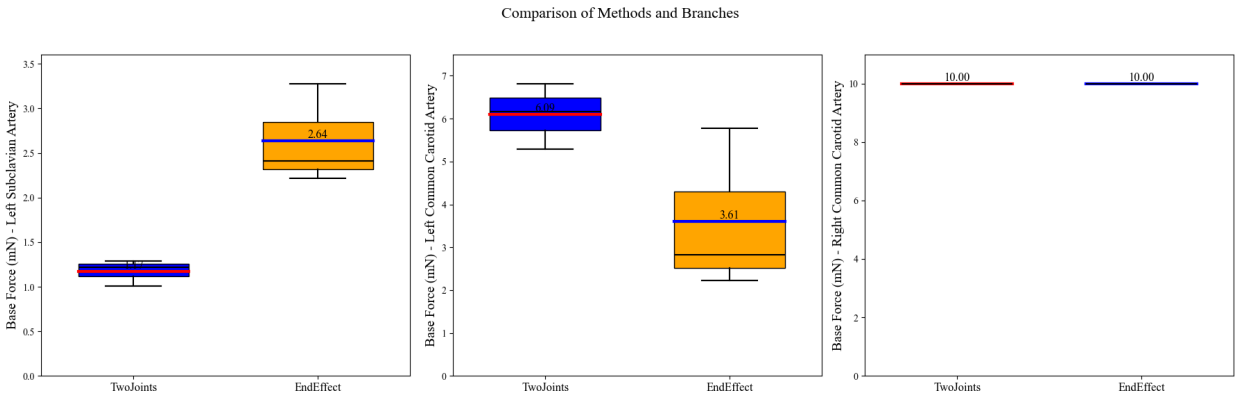

Figure 39: Base force from experienced users

Figures 36 and 37 show the average tip force for the Inexperienced and Experienced users respectively to navigate to the LSA, LCCA and RCCA. Figures 38 and 39 show the same data but for the base force. For the purposes of analysis, when a user fails to complete the task within the allotted time, the tip force and base force will be recorded as 15mN and 10mN respectively. 15mN and 10mN refers to the safety threshold applied in this study.

The mean maximum force at tip of 'Two Joints Controller' for LSA, LCCA and RCCA was 3.81/3.91mN, 8.65/4.53mN and 10.63/15mN respectively, and it turned to be 3.69/4.27mN, 8.33/5.00mN and 9.15mN/15mN for End Effect Controller. Meanwhile, the mean maximum force at base of 'Two Joints Controller' for LSA, LCCA and RCCA was 1.56/1.17mN, 3.20/6.09mN and 8.22/10mN respectively, and it turned to be 1.78/2.64mN, 6.17/3.61mN and 8.47mN/10mN for End Effect Controller.

Mean maximum force / mN					
		Participants	LSA	LCCA	RCCA
Tip Force	Two joints	students	3.81	8.65	10.63
		Experienced users	3.91	4.53	15
	End Effect	students	3.69	8.33	9.15
		Experienced users	4.27	5.00	15
Base Force	Two joints	students	1.56	3.20	8.22
		Experienced users	1.17	6.09	10
	End Effect	students	1.78	6.17	8.47
		Experienced users	2.64	3.61	10

Table 3: Mean maximum tip/base force Data by human operation

5.2.4 Qualitative Result

Figure 40 presents the qualitative results collected from the participants, each plot corresponds to the responses from the participants on a 5-point Likert scale. The questions were designed to assess the two control modes on several aspects including system responsiveness, feedback realism, control intuitiveness, precision and anatomical accuracy. The responses were collected from 3 inexperienced users and 1 experienced user. The scale ranges from 1 (Strongly Disagree) to 5 (Strongly Agree).

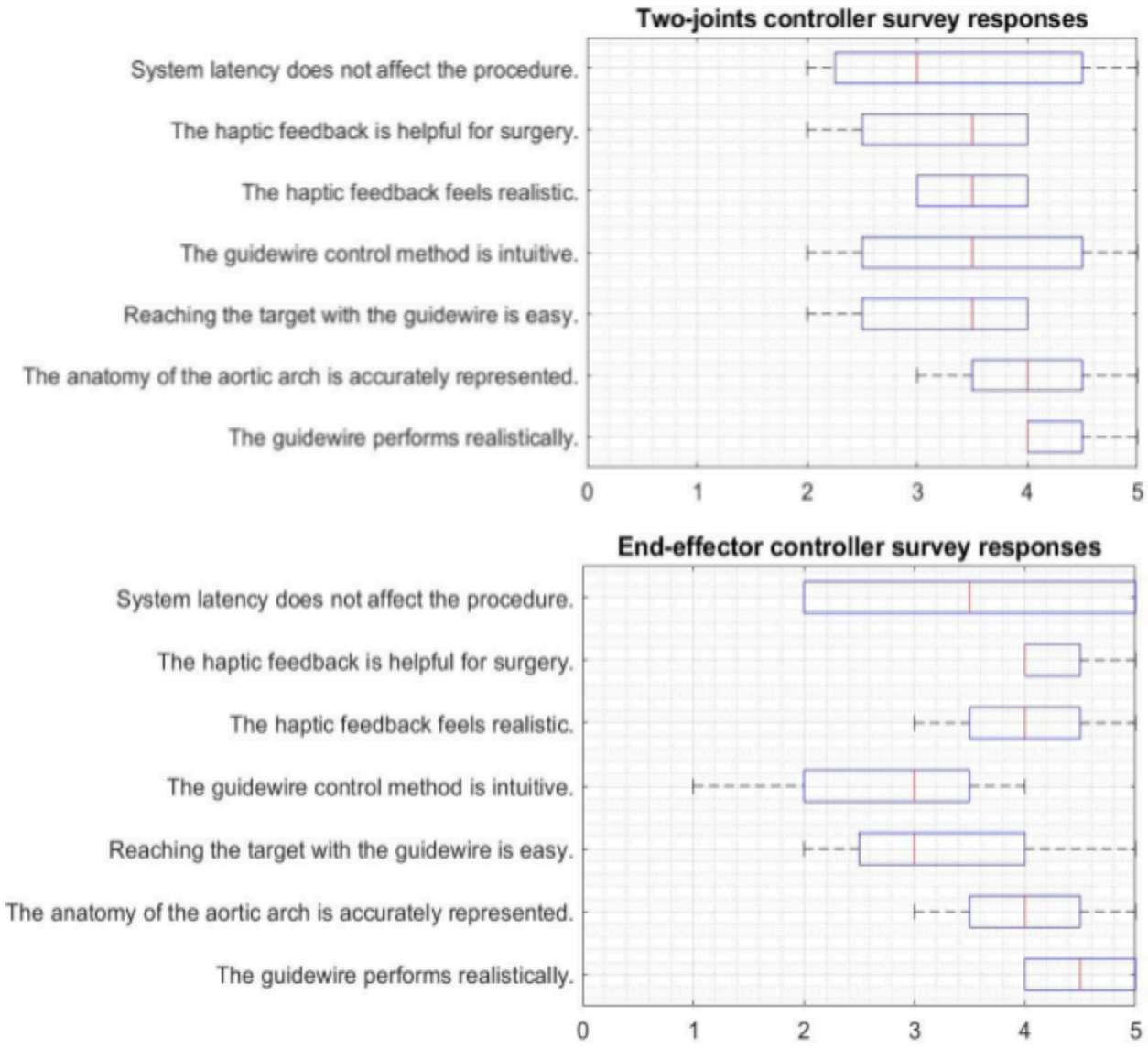

Figure 40: Box plots showing responses for the survey regarding the End-effector controller (Top) and the Two joints controller (Bottom).

The impact of system latency on the procedure is similar across the two controller modes, indicating consistent system performance.

In comparison with the two joints mode, the end-effect got a higher mark for haptic feedback realism, which indicates the third joint could potentially be a better site to apply haptic feedback. Both modes receive relatively low marks for the intuitiveness, the end-effect method was evaluated as a less intuitive method with a median score of 3.25.

Participants rated the haptic feedback from the end-effector controller as more helpful for surgery, with a mean score of 4.25. The result might not accurately reflect the usefulness of the haptic feedback since participants lacked surgical experience. Due to similar reasons, even though the accuracy of the anatomy score 4 and 4 for end-effector and two joints control modes respectively, the result may not represent the accuracy of the anatomy.

The realism of the guidewire got the highest grade, this suggests that the simulation successfully replicates the dynamics of a real guidewire, making it a highly effective toolkit for the development of tele-operated techniques.

5.3 Reinforcement Learning

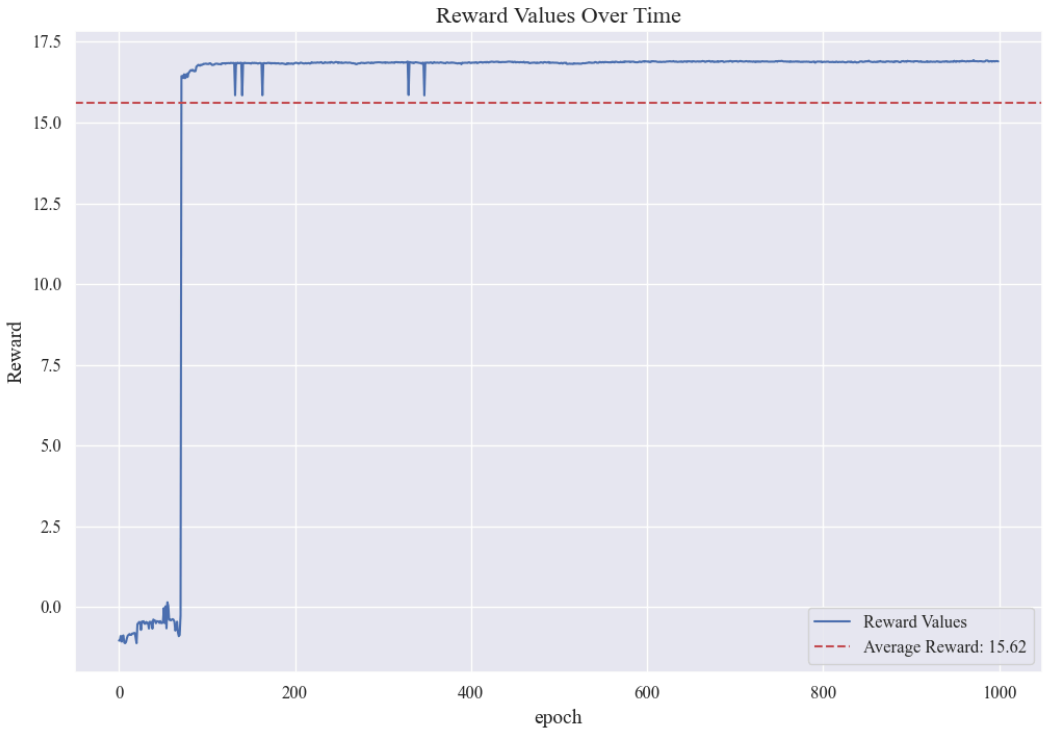

Figure 41: Cumulative reward over time during reinforcement learning training process

Figure 41 shows how the reward values change over time steps during training of the model. Initially the reward value is staying below 0 and fluctuating, but rises rapidly and stabilises after about 100 epochs, remaining at a high level about 17. The average reward is 15.62. We can find that the reward values are above average for most of the time. This suggested that the model performs well on most of the time-steps and has learnt an effective and stable strategy.

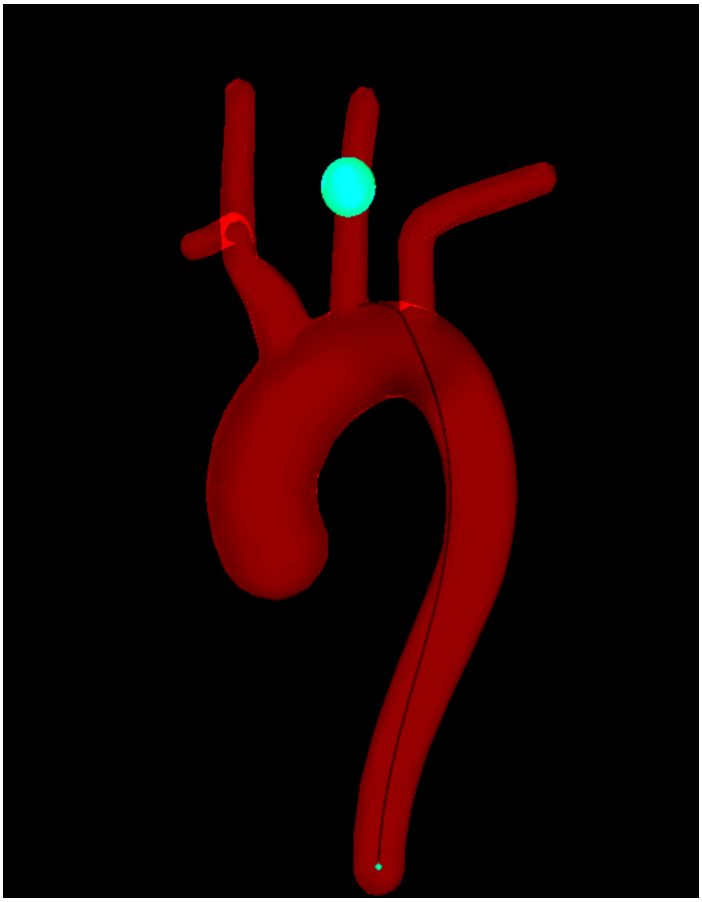

Figure 42: Autonomous Navigation in the Blood Vessel

Figure 42 shows the progress of a guidewire navigating during a reinforcement learning training session. The green marker represents the target position within the vascular structure

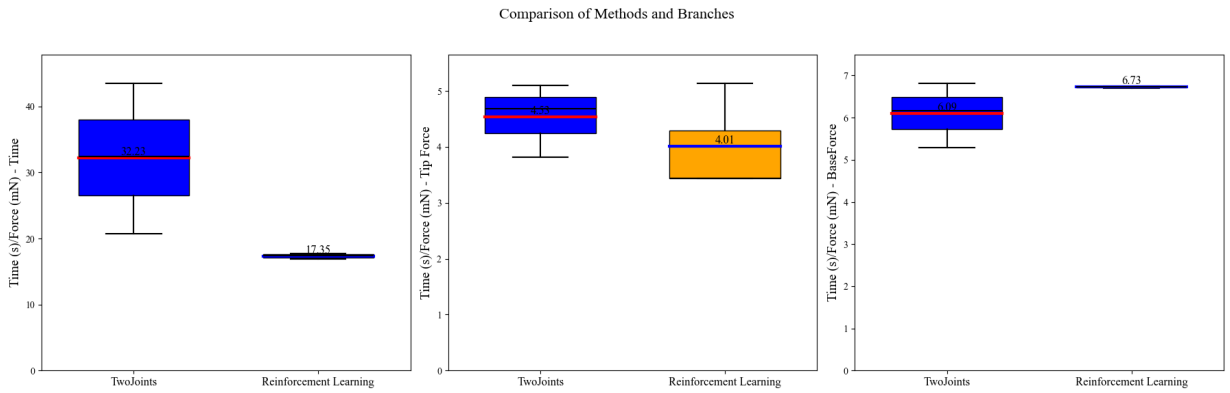

Figure 43: Comparison of Performance on LCCA(Left Common Carotid Artery) between experiences users and reinforcement learning algorithm

Figure 43 compares the performance of the manually operated Two-Joints controller with the performance of the reinforcement learning algorithm specifically in regards to the navigation of the LCCA. The Two-Joints controller was selected for this evaluation as it scored the highest in the survey for intuitive controls. Furthermore, upon consulting clinician about the clinical significance of different branches, we discovered that the RCCA has similar clinical significance as LCCA, however, we chose to focus on the navigation of the LCCA. This is because clinicians also stated that LCCA tends to be the most challenging branch to navigate during neurointerventional procedures. The reason for this is likely due to the changes in neuroanatomy in patients of advanced age. Elderly patients tend to have LCCAs that first curve downwards before curving upwards [29].

The average time for the reinforcement learning algorithm to navigate the LCCA was approximately 17.35 seconds, much lower than that of manual operation by which is 32.23

seconds (P = 0.0868). The average tip force produced by the reinforcement learning method is about 4.01 mN , this is lower than that of the Two-Joints controller at 4.53 mN (P = 0.4858). However, the reinforcement learning model was trained and tested on the same vascular mesh. This may potentially introduce bias to the results towards favourable outcomes for the algorithm. limitations exist since the experiment does not provide a robust evaluation of the algorithm's generalizability to different anatomical variations it has not encountered before.

Whereas tip force produced by the reinforcement learning algorithm is lower than that of manually operated controllers, base force is overall higher. This offers interesting insights into the effectiveness of the reinforcement learning algorithm, when considering the risk of damage to the vessels. Complete puncture of the caudal cardiac vessels, including the aortic branch, LCCA, RCCA and the Left Subclavian artery are unlikely. However it is possible for minimally invasive procedures which use a catheter to cause dissection of vessels, causing the separation of the vessel layers and consequently putting the patient at risk of stroke [33]. Given this risk is increased with higher tip force, the reinforcement learning algorithms tendency towards lower tip forces and higher base forces provides an advantage in reducing risk of recurrence in patients. Furthermore, it could be argued the End-Effector controller also provides a lower risk of recurrence in comparison with the Two-Joints controller.

5.4 Clinician Testing

Given there are only around 80 clinicians in the UK qualified to carry out remote thrombectomy, evaluating the efficacy of the controllers alongside practising clinicians is of utmost importance. Within this study we were able to have one clinician, a neurointerventional radiologist, test the controller. The results of which are shown below:

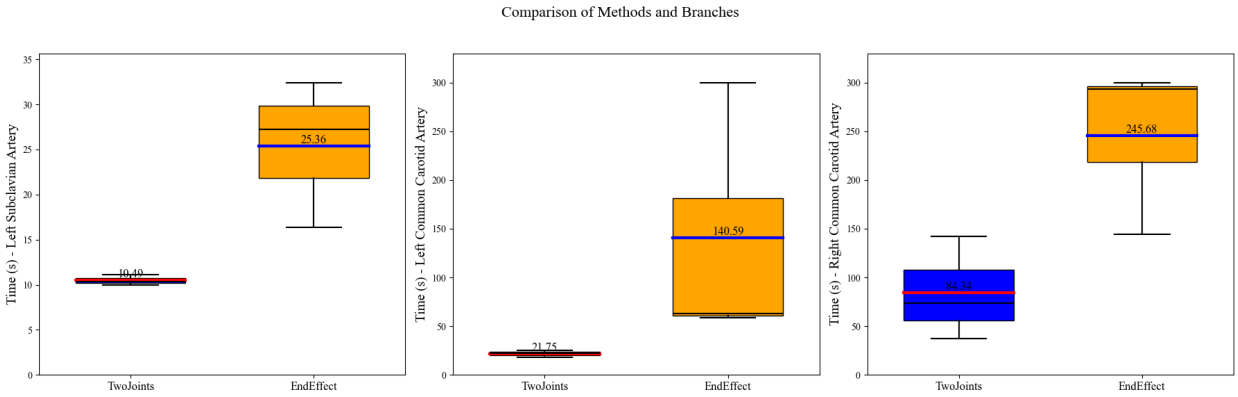

Figure 44: Results of clinician testing using haptic Two-Joints and End Effector controller.

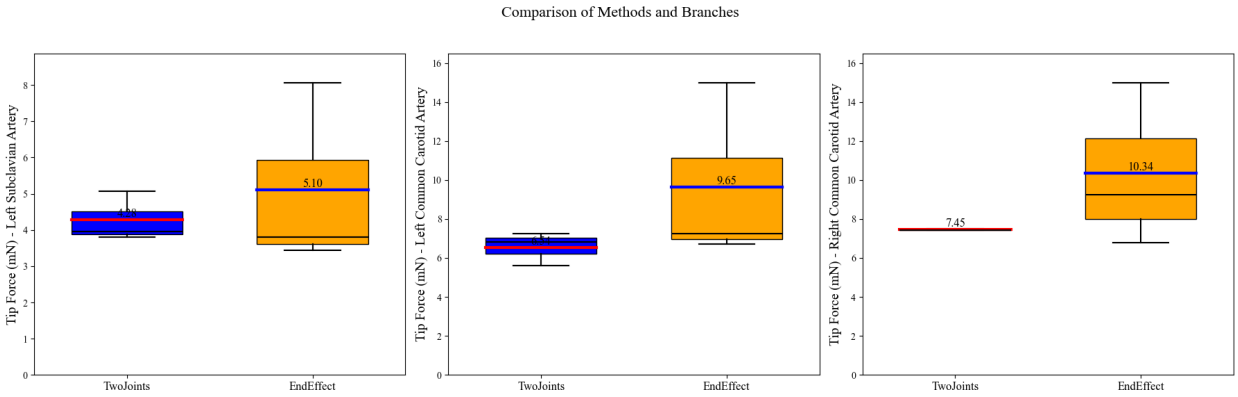

Figure 45: Tip Force for clinician users reaching target of different branches

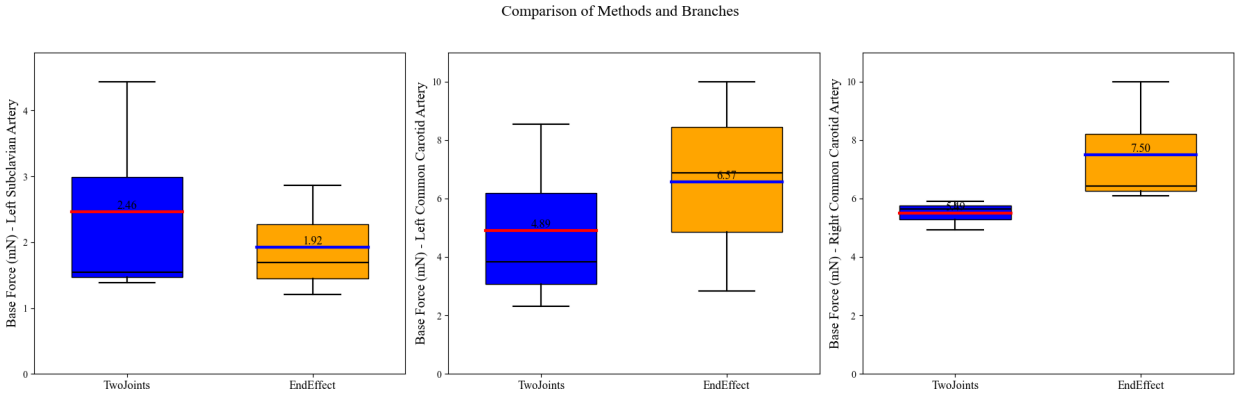

Figure 46: Base Force for clinician users reaching target of different branches

It can be observed that the clinician's performance is extremely different when compared with that of the Inexperienced and Experienced users. For all three arteries, the clinician when using the Two-Joints haptic controller completed the navigation in significantly less time (P = 0.0415), than when using the End-effector controller.

Participaters	Time / s	Tip Force / mN	Base Force / mN
Clinician Users	21.75	6.54	4.89
Reinforcement Learning	17.35	4.01	6.73

Table 4 : Data comparison between Experts Users and Reinforcement Learning

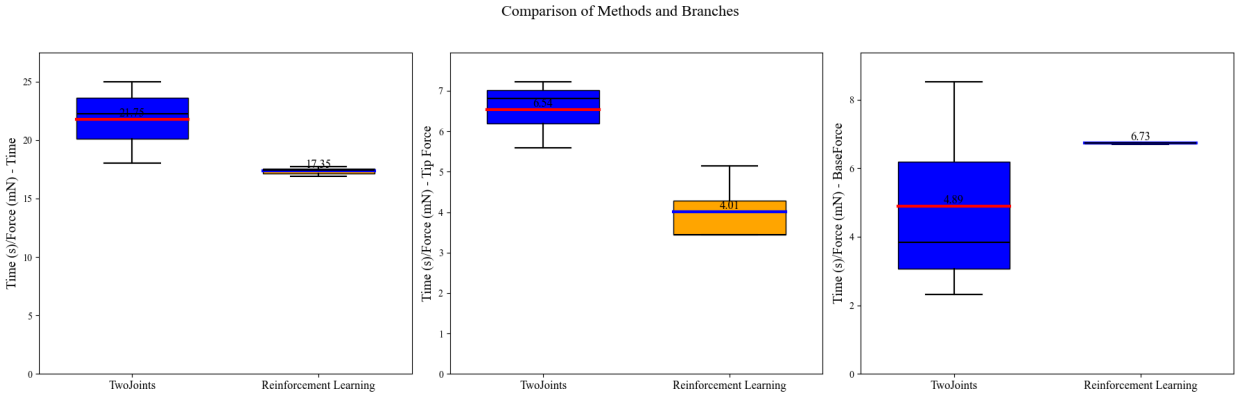

Figure 47: Comparison of Performance on LCCA between clinician users and reinforcement Learning algorithm

When we compare the clinicians performance using the Two-Joints controller with the performance of the reinforcement learning algorithm, we can see that the reinforcement learning completed the navigation on average quicker than the clinician using the Two-Joints controller (P= 0.4266) with the two control methods having mean times of 17.35s and 38.86 seconds respectively.

In terms of force, when being used by the clinician, the Two-Joints haptic controller exerted less tip force than the End-Effector haptic controller (P = 0.1454) with mean tip forces of 6.09mN and 8.36mN respectively. It is noteworthy that both of these values are under the safe threshold value of 15mN. A similar pattern is observed with base force, when being used by the clinician, the Two-Joints haptic controller exerted less base force than the End-Effector haptic controller (P = 0.4510) with mean tip forces of 4.28mN and 5.33mN respectively.

When we compare the base force used by the reinforcement learning algorithm with the tip force exerted by the clinician using the Two-Joints controller we see that overall the force exerted by the Two-Joints controller when used by the clinician is lower (P = 0.1063), with the reinforcement learning exerting on average 6.73mN. However tip force exerted by the clinician is higher (P = 0.0534), with the reinforcement learning exerting on average 4.01mN.

5.5 Materials Testing Results

The results of the Instron Machine testing are described below. The Young's Modulus was calculated using *Equation 1* as described in section 4.1.3.

Sample	Force (kN)	Length (mm)	Extension (mm)	Area (mm^2)	Young's Modulus
SrirayaTech Lumen	0.02	90	108	14.92	1.12MPa
SrirayaTech Rectangle	0.05	70	23.85	15	9.98MPa
Formlabs Lumen	0.01	50	33.55	22.78	0.654MPa
Formlabs Rectangle	0.02	30	40.91	15	0.978MPa

Table 5: results of materials testing for printing materials under consideration

The literature values for the Young's Modulus of the carotid artery are between 700 - 980kPa [24], when compared to the values calculated we see that whereas the SrirayaTech Tenacious

resin Young's Modulus values are still too high, when FormLabs Elastic 50A resin is washed and only partially cured it produces a material which falls within range. It is important to note that as these samples were taken directly from phantoms there will likely be variation in their material properties as they were never entirely cured. Consequently, depending on the storing conditions these phantoms were subjected to between printing and being tested, variations in exposure to ambient UV could vary. This most likely explains the significant difference between the Young's Modulus values for the SrirayaTech Tenacious Clear samples.

5.6 Ethics and Regulations

Within this section, we explore the ethical concerns associated with the manufacture and implementation of the proposed device detailed within this paper. In terms of the use of patient data to create the 3D phantom, anonymised patient data was used to avoid the breach of privacy law. Furthermore, the mesh used to train the reinforcement learning algorithm was randomly generated.

It is important to consider what regulations would apply to the device, as there is very little precedent for remotely operated medical devices, and the logistics regarding liability. Since leaving the EU in 2020, the relevant regulations are the UK MDR (Medical Devices Regulations). Within these regulations, the device detailed within this project would most likely fall under Class III and would require extensive clinical evidence before being approved for use.

6 Limitations

6.1 3D Phantom

6.1.1 Image resolution

As the segmentations used to create the phantom are extracted from CT scans, the details of the segmentations extracted are limited by the resolution of the images provided. This manifested in a limitation regarding how thin the model walls can be when hollowed via 3D slicer, requiring the use of Blender to produce thin walls. Furthermore, the resolution of the CT images also led to the merging of vessels that were too close to one another, as seen in Figure 48.

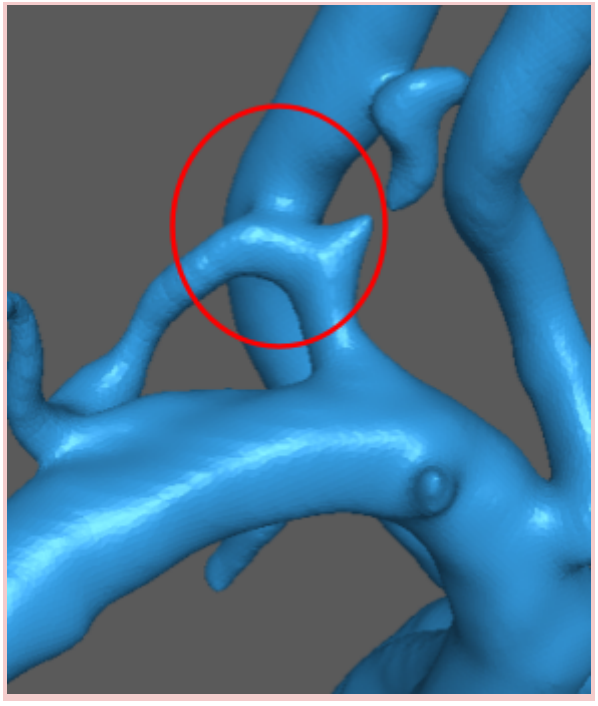

Figure 48: An image of two vessels merging during segmentation.

Errors like this needed to be corrected manually, which compromises the accuracy of the final model. Furthermore, the contrast offered by the CT scans is extremely limited, especially in the superior sections of the head. Extracting neurovascular segmentations in these regions proved difficult, with many of the CT scans not having enough contrast for proper segmentation as seen in Figure 49.

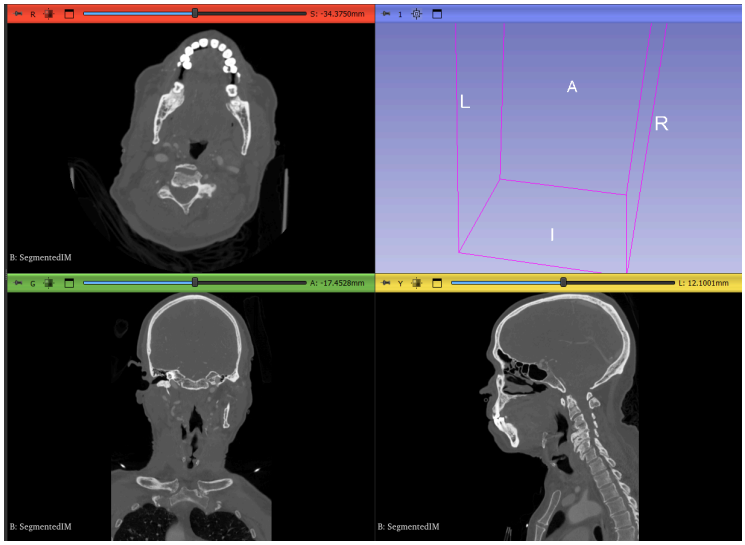

Figure 49: Image of lower contrast, especially in superior axial regions.

6.1.2 Resin Availability

The Young's modulus of the carotid artery in those at risk of atherosclerosis ranges from 700 - 980 kPa [24]. Few resins produce final products within that range, with the softest resin types available from SrirayaTech and FormLabs having Young's Moduli of 800MPa and 1.5MPa [25][26] respectively. Hence the closest matching resin would be over 50% more elastic than the

actual values. Even though the resins were left entirely or partially uncured in attempts to reduce this value, over time the exposure to ambient light during storage and testing causes the resin to harden further.

6.1.3 Printer Dimensions and Resolution

Due to the dimensions of the vasculature being represented, a printer bed of minimum (280mm x 130mm x 280mm) dimensions is required. Very few printers can create models of that size, which further limits the choice of resins that are available as not all printers and resin types are compatible with one another.

The use of smaller printers was considered, however, this increased post-processing and introduced several issues. Firstly, when using smaller printers, it is often required to scale down the segmentation. This process makes the final product less accurate and can lead to vasculature becoming more narrow than it would be in reality. In instances where the model is sliced and printed in portions, manually combining the sections can prove difficult and often led to striations in the phantom which impede the movement of the catheter. The process of combining smaller sections also introduces more UV to the phantom which hardens it and causes irregular mechanical properties at sites of connection.

6.1.4 Printer settings and supports

As neurovasculature can become quite narrow, there was a high risk of UV from the LCD screen sealing the vessels shut or trapping resin inside during printing. This would cause certain sections of the print to be extremely hard as the resin cured over time.

One significant limitation is the fragility of the phantom. As the phantom must be soft and flexible but also entirely hollow it is not well-suited for heavy supports. This is because adding supports throughout the model requires placing supports inside the model. Due to the shape of the model these supports are extremely difficult to remove after the print has been completed without causing damage to the print itself. Adding supports for narrower vessels can also lead to the vessels being sealed shit. Printing the model using sparse supports risks the partial or complete collapse of the phantom.

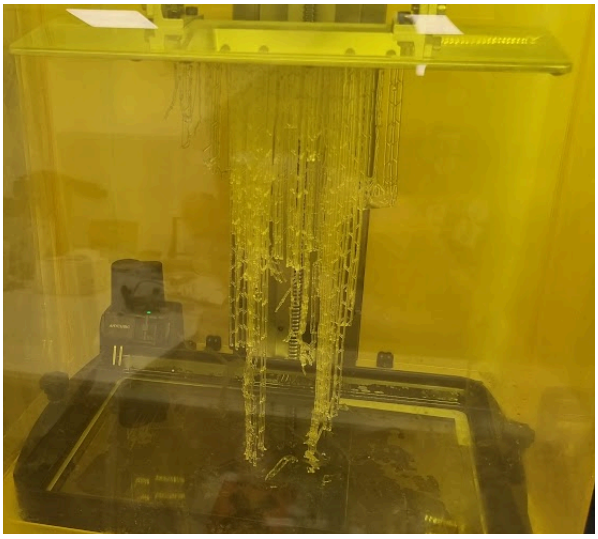

Figure 50: Collapsed phantom on printing bed

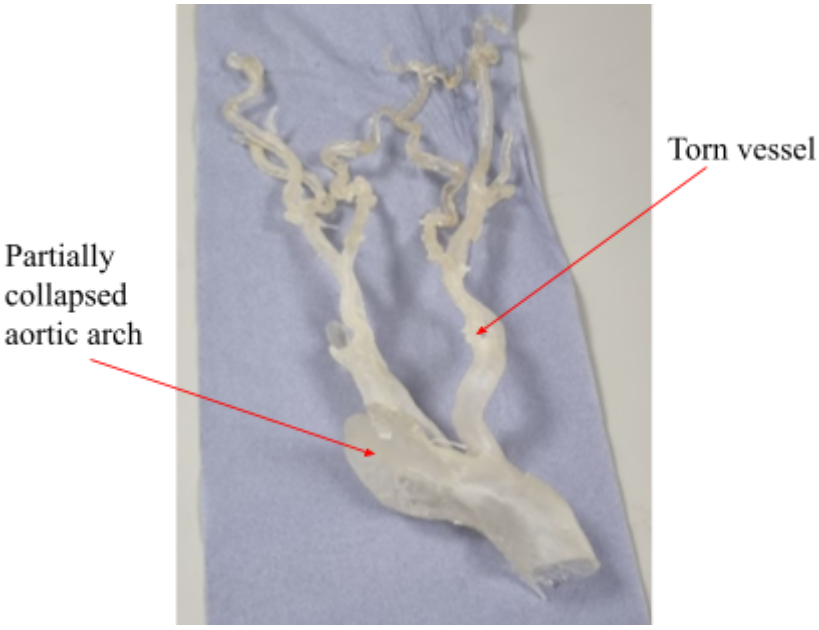

Figure 51: Partially collapsed phantom after post-processing procedure

6.2 Haptic controller

6.2.1 3D Printer

An FDM BambuLab X1C printer was used to print the components of the controller. BambuLab X1C has a build size of 400x400x400 mm, which limits the printer's ability to print very large components such as the controller base in a single run.

Aside from the size constraints, the 3D printed components have limited accuracy due to unevenness caused by the striations of the different layers, as shown in Figure 52 . To improve this, printing parameters such as layer height and print speed were adjusted across several iterations. Despite these changes, flatness issues persisted, which has led to misalignment and gaps during the assembly process.

Figure 52 :Surface Unevenness in 3D Printed Components

6.2.2 Flexible Circuit

The brushless motor used in the project is equipped with a flexible circuit (Figure 53). The flexible circuit offers advantages in terms of reduced size and weight, along with enhanced flexibility.

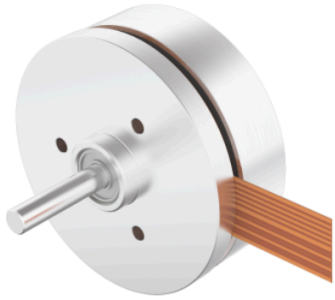

Figure 53: Flexible Circuit in RS Pro 2163794 Brushless Motor

However, there are limitations caused by the main circuit board being incompatible for direct integration with flexible circuits. Connectors are required to bridge these systems, which increase the complexity and cost. This use of connectors also offsets the advantages offered by flexible circuits. Furthermore, flexible circuits are relatively fragile, they are more likely to be damaged during operation, leading to increased maintenance requirements.

6.3 Reinforcement Learning

A significant limitation of the reinforcement learning aspect of the project is the lack generalizability of the algorithm itself. This is due to the highly specific training data the algorithm has been trained on, having been trained exclusively on a specific mesh. The algorithm would most likely not perform well on an unfamiliar mesh. This also contributes to the algorithm's lack of robustness.

Furthermore, the interpretability of the system, which refers to how well an observer can track cause and effect within a system, is significantly low due to the nature of general machine learning. The algorithm itself acts as a ‘black box’ and via several layers of neural networks outputs results that are impossible to track or justify.

The training process is also somewhat inefficient and has a large computational time, the process requires a large amount of data, and has approximately millions of steps. This issue is further exacerbated by the limitations of the GPU and CPU that the algorithm is being run on, with the Nvidia RTX 4060 having 8GB of memory.

7 Future Works

7.1 3D Phantom

7.1.1 Image resolution

To resolve the issue of limited image resolution and contrast, making use of 3D angiography scans could benefit future studies. Angiography scans provide high-contrast detailed images of the vasculature which could be integrated into existing segmentations. This would allow us to better represent the circle of Willis and complex cerebral neuroanatomy.

7.1.2 Recommended resin and printing protocol

For future works, a large printer compatible with FormLabs Elastic 50A Resin is recommended. The print should be rinsed and cured for 10-15 minutes, to retain a lower Young's Modulus but reduce tackiness which would make the print difficult to handle and prone to tearage. After the supports of the print are removed, storing the print in a dark area would reduce the amount of curing caused by ambient light before testing can take place. Submerging the phantom in glycerin during testing would allow for an environment compatible both with the catheter apparatus and imaging modalities.

7.1.3 Synthetic clot formulation

Previous studies exploring the production of synthetic clots use agarose-based and silicone-based mixtures. To simulate calcification, 3D structures can be added to clots. Studies show a mixture of agarose and MCI*/MI** act as a reliable base for synthetic clots which simulate arterial clots. Silicone and MCI/MI mixtures can be used to simulate venous clots. MGB (micro-glass beads) can be added to simulate mixed clots [27].

* A 3:1 mixture of methylchloroisothiazolinone (MCI)

** A 3:1 mixture of methylisothiazolinone (MI)

Future works should move towards phantom development that includes blood clot analogues manufactured using agarose and silicone mixtures.

7.2 Haptic Controller

7.2.1 Semi-simulation Experiment

For future work on the development of the haptic controller, it is recommended to focus on software and hardware integration, to integrate the developed haptic controller as a control interface of the SOFA simulation platform. This integration facilitates semi-simulation experiments, which can bridge the gap between virtual simulations and in vitro experiments.

By conducting these experiments, we can evaluate the enhanced precision of the haptic controller, provided by the hardware development in this study. Furthermore, these semi-simulation experiment results could be compared with those obtained in this study using the Plane Scara robot.

This comparative analysis would provide valuable insights into the effectiveness of the controller in providing haptic feedback, potentially leading to significant improvements in tele-operated thrombectomy.

7.2.2 6 DOF Haptic controller

For future work, it’s also recommended to consider developing a 6 DOF haptic controller. This advancement would significantly enhance the existing 2DOF system by providing a more comprehensive range of haptic feedback.

A 6 DOF system can provide a more intuitive control, such as pitching, yawing, rolling, and translating along three perpendicular axes. This level of control is crucial for navigating the guidewire in complex vascular structures. This may potentially enhance the surgeon's manoeuvrability and the realism of the haptic feedback.

7.3 Reinforcement Learning

In the future the algorithm could be improved by training on more diverse meshes. This would increase the generalizability of the mesh, allowing it to be reliable on a number of varied anatomies. Furthermore, adding a force punishment term to the reward function would greatly benefit the algorithm. In doing this, the force applied by the virtual guidewire to the vasculature would be minimised. A lower amount of force not only better mimics the cautious behaviours of a human clinician but also makes the procedure safer overall.

Future works should also aim to evaluate the performance of the controllers when being used by a more significant proportion of qualified clinicians. Within this study we were only able to have one clinician, a neurointerventional radiologist, test the controller, which reduced the clinical significance of the results .

8 Discussion and Conclusions

In conclusion, this study focused on creating several deliverables which contribute towards a toolkit for the development of a tele-operated remote thrombectomy procedure.

The project met the majority of its primary objectives in the development of a toolkit for remote thrombectomy; two haptic feedback controllers were manufactured, a reinforcement learning

algorithm was created which was able to carry out the first steps of a thrombectomy procedure, and whereas a full 3D vascular phantom was not successfully printed, the segmentation was successfully converted into a compatible mesh which can be used for future experimentation.

This project was limited by smaller sample sizes and a lack of in-vitro experiments which restricted any assessment made of the practicality of implementing the device in a clinical setting. Future works should focus on completing the construction of the phantom, using guidance included in section 7.1 and carrying out in vitro testing with a larger sample size. Changes to the reinforcement learning algorithm including a force punishment term would also greatly improve the project. Furthermore, experiments to assess the performance of the reinforcement learning algorithm across different anatomical variations will also provide insights into its robustness in different clinical settings.

The findings of this project are novel as there are very few similar studies, with only one relevant study published in 2023. Within this study, there was no use of reinforcement learning and only one haptic controller was designed [10]. The impact of this work lies in the detailed methodologies provided in it which lay the foundation for experimentation surrounding remote endovascular procedures, which benefit the global community by laying the foundation for wider accessibility to emergency neurointerventional procedures worldwide.

References

1. Stroke Association (2024). *Stroke Statistics*. [online] www.stroke.org.uk. Available at: https://www.stroke.org.uk/stroke/statistics.
2. www.stroke.org.uk. (n.d.). *Ischaemic stroke | Stroke Association*. [online] Available at: https://www.stroke.org.uk/stroke/types/ischaemic#:~:text=It.
3. Marchese, G., Prochazka, B. and Widimsky, P. (2016). The importance of time: Time delays in acute stroke. *Cor et Vasa*, [online] 58(2), pp.e225–e232. doi:https://doi.org/10.1016/j.crvasa.2016.03.002.
4. White, P.M., Alton, A., James, M., Price, C., Shaw, L., Flynn, D., Burgess, D., McMeekin, P. and Ford, G.A. (2023). Research letter: An updated survey of intra-arterial mechanical thrombectomy service provision in England. *European Stroke Journal*, p.239698732311674. doi:https://doi.org/10.1177/23969873231167452.
5. Marchese, G., Prochazka, B. and Widimsky, P. (2016). The importance of time: Time delays in acute stroke. *Cor et Vasa*, [online] 58(2), pp.e225–e232. doi:https://doi.org/10.1016/j.crvasa.2016.03.002.
6. Anon, (2022). *Ethnicity and Stroke | Different Strokes*. [online] Available at: https://differentstrokes.co.uk/ethnicity-stroke/.
7. Lindmark, A., Eriksson, M. and Darehed, D. (2022). Socioeconomic status and stroke severity: Understanding indirect effects via risk factors and stroke prevention using innovative statistical methods for mediation analysis. *PLOS ONE*, 17(6), p.e0270533. doi:https://doi.org/10.1371/journal.pone.0270533.
8. Wei, Y., Bordas, S., Jeremie Dequidt, Duriez, C., Allard, J. and Erwan Kerrien (2012). A (Near) Real-Time Simulation Method of Aneurysm Coil Embolization. doi:https://doi.org/10.5772/48635.
9. Crinnion, W., Jackson, B., Sood, A., Lynch, J., Bergeles, C., Liu, H., Rhode, K., Pereira, V.M. and Booth, T.C. (2022). Robotics in neurointerventional surgery: a systematic

review of the literature. *Journal of NeuroInterventional Surgery*, [online] 14(6), pp.539–545. doi:https://doi.org/10.1136/neurintsurg-2021-018096.

10. Jackson, B., Crinnion, W., De, M., Robertshaw, H., Christos Bergeles, Rhode, K. and Booth, T. (2023). Comparative verification of control methodology for robotic interventional neuroradiology procedures. *International Journal of Computer Assisted Radiology and Surgery*, 18(11), pp.1977–1986. doi:https://doi.org/10.1007/s11548-023-02991-2.
11. Robertshaw, H., Lennart Karstensen, Jackson, B., Hadi Sadati, Rhode, K., Sebastien Ourselin, Granados, A. and Booth, T.C. (2023). Artificial intelligence in the autonomous navigation of endovascular interventions: a systematic review. *Frontiers in human neuroscience*, 17. doi:https://doi.org/10.3389/fnhum.2023.1239374.
12. Campbell, B.C.V., De Silva, D.A., Macleod, M.R., Coutts, S.B., Schwamm, L.H., Davis, S.M. and Donnan, G.A. (2019). Ischaemic stroke. *Nature Reviews Disease Primers*, 5(1). doi:https://doi.org/10.1038/s41572-019-0118-8.
13. Brain Research UK (2021). *Stroke – Neurological condition*. [online] www.brainresearchuk.org.uk. Available at: https://www.brainresearchuk.org.uk/neurological-conditions/stroke.
14. Anon, (n.d.). *Aortic Arch | neuroangio.org*. [online] Available at: https://neuroangio.org/anatomy-and-variants/aortic-arch/ [Accessed 1 Jun. 2024].
15. Mangiardi, M., Bonura, A., Iaccarino, G., Alessiani, M., M. Bravi, Crupi, D., Francesca Romana Pezzella, Fabiano, S., Enrico Pampana, Stilo, F., Alfano, G. and Anticoli, S. (2023). The Pathophysiology of Collateral Circulation in Acute Ischemic Stroke. *Diagnostics*, 13(14), pp.2425–2425. doi:https://doi.org/10.3390/diagnostics13142425.
16. NHS (2017). *Stroke - Recovery*. [online] nhs.uk. Available at: https://www.nhs.uk/conditions/stroke/recovery/#:~:text=Strokes%20can%20cause%20weakness%20or.
17. Clinical Commissioning Policy: Mechanical thrombectomy for acute ischaemic stroke (all ages). (n.d.). Available at:

https://www.england.nhs.uk/wp-content/uploads/2019/05/Mechanical-thrombectomy-for-acute-ischaemic-stroke-ERRATA-29-05-19.pdf.

18. Mathews, S. and De Jesus, O. (2020). *Thrombectomy*. [online] PubMed. Available at: https://www.ncbi.nlm.nih.gov/books/NBK562154/.
19. Catapano, J.S., Kavelin Rumalla, Farhadi, D.S., Parikh, P., Nguyen, B.A., Rutledge, C., Srinivasan, V.M., Baranoski, J.F., Cole, T.S., Winkler, E.A., Desai, S.M., Ducruet, A.F., Albuquerque, F.C. and Jadhav, A.P. (2022). Safety and Efficacy of Radial Versus Femoral Artery Access for Mechanical Thrombectomy Procedures Following Intravenous Administration of Tissue Plasminogen Activator. *Stroke: vascular and interventional neurology*, 2(5). doi:https://doi.org/10.1161/svin.121.000238.
20. Rana, N., Vijayvergiya, R., Kasinadhuni, G., Khanal, S. and Panda, P. (2021). Comparison of radial versus femoral access using hemostatic devices following percutaneous coronary intervention. *Indian Heart Journal*. doi:https://doi.org/10.1016/j.ihj.2021.04.006.
21. D'Souza, D. (n.d.). *Bovine arch | Radiology Reference Article | Radiopaedia.org*. [online] Radiopaedia. Available at: https://radiopaedia.org/articles/bovine-arch?lang=gb.
22. uk.rs-online.com. (n.d.). *Bosch Rexroth R060230810, Bearing with 16mm Outside Diameter | RS*. [online] Available at: https://uk.rs-online.com/web/p/linear-bearings/4893985?gb=s [Accessed 1 Jun. 2024].
23. uk.rs-online.com. (n.d.). *RS PRO Brushless DC Motor, 12 V dc, 0.16 Nm, 2910 rpm, 4mm Shaft Diameter | RS*. [online] Available at: https://uk.rs-online.com/web/p/dc-motors/2163794 [Accessed 1 Jun. 2024].
24. Riley, W.A., Barnes, R.W., Evans, G.W. and Burke, G.L. (1992). Ultrasonic measurement of the elastic modulus of the common carotid artery. The Atherosclerosis Risk in Communities (ARIC) Study. *Stroke*, 23(7), pp.952–956. doi:https://doi.org/10.1161/01.str.23.7.952.
25. Domingo-Roca, R., Asciak, L., Windmill, J.F.C., Mulvana, H. and Jackson-Camargo, J.C. (2022). Non-destructive Analysis of the Mechanical Properties of 3D-Printed Materials.

Journal of Nondestructive Evaluation, [online] 41(1). doi:https://doi.org/10.1007/s10921-022-00854-5.

26. Siraya Tech. (n.d.). *Flexible - Tenacious Resin User Guide*. [online] Available at: https://siraya.tech/pages/tenacious-user-guide [Accessed 1 Jun. 2024].
27. Guerreiro, H., Wortmann, N., Andersek, T., Ngo, T.N., Frölich, A.M., Krause, D., Fiehler, J., Kyselyova, A.A. and Flottmann, F. (2022). Novel synthetic clot analogs for in-vitro stroke modelling. *PloS one*, [online] 17(9), pp.e0274211–e0274211. doi:https://doi.org/10.1371/journal.pone.0274211.
28. *Subclavian artery* (2024) *Wikipedia*. Available at: https://en.wikipedia.org/wiki/Subclavian_artery (Accessed: 01 June 2024).
29. V. Kamenskiy, A. (2015). Age and disease-related geometric and structural remodeling of the carotid artery. *Journal of Vascular Surgery*, [online] 62(6), pp.1521–1528. doi:https://doi.org/10.1016/j.jvs.2014.10.041.
30. Schulman, J. *et al.* (2017) *Proximal policy optimization algorithms*, *arXiv.org*. Available at: https://arxiv.org/abs/1707.06347 (Accessed: 01 June 2024).
31. *Reinforcement learning: An introduction*. Available at: https://web.stanford.edu/class/psych209/Readings/SuttonBartoIPRLBook2ndEd.pdf (Accessed: 01 June 2024).
32. *Bosch Rexroth R060230810, bearing with 16mm outside diameter* (no date) *RS*. Available at: https://uk.rs-online.com/web/p/linear-bearings/4893985?gb=s (Accessed: 02 June 2024).